



HAL
open science

Platinum-nickel nanowires and nanotubes arrays as carbon-free cathodes for the PEM fuel cell

Othman Lagrichi, Laure Guetaz, Olivier Sicardy, Denis Buttard, Arnaud Morin

► **To cite this version:**

Othman Lagrichi, Laure Guetaz, Olivier Sicardy, Denis Buttard, Arnaud Morin. Platinum-nickel nanowires and nanotubes arrays as carbon-free cathodes for the PEM fuel cell. ACS Applied Energy Materials, 2023, 2 (5), pp.11997-12012. 10.1021/acsaem.2c01231 . cea-03813207

HAL Id: cea-03813207

<https://cea.hal.science/cea-03813207>

Submitted on 13 Oct 2022

HAL is a multi-disciplinary open access archive for the deposit and dissemination of scientific research documents, whether they are published or not. The documents may come from teaching and research institutions in France or abroad, or from public or private research centers.

L'archive ouverte pluridisciplinaire **HAL**, est destinée au dépôt et à la diffusion de documents scientifiques de niveau recherche, publiés ou non, émanant des établissements d'enseignement et de recherche français ou étrangers, des laboratoires publics ou privés.

Platinum-Nickel Nanowires and Nanotubes Arrays as Carbon-free Cathodes for the PEM Fuel Cell

Othman. Lagrichi^{‡†}, Laure Guétaz[‡], Olivier Sicardy[‡], Denis Buttard[†], Arnaud Morin[‡]

[‡]Univ. Grenoble Alpes, CEA, Liten, DEHT, STP, F-38000 Grenoble, France

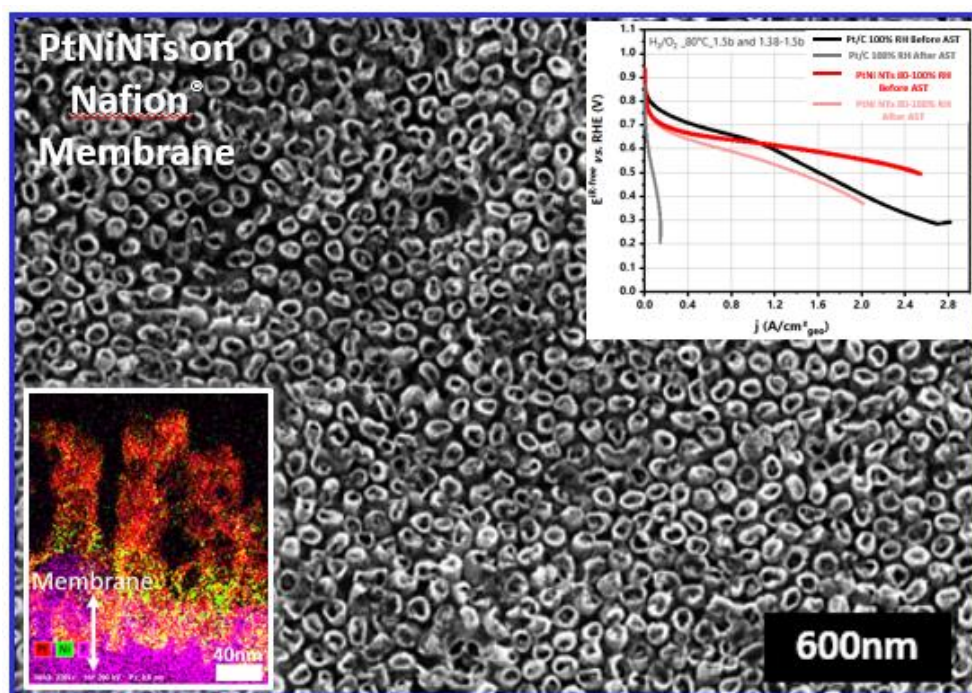
[†] Univ. Grenoble Alpes, CEA, IRIG, Pheliqs, SiNaPS, F-38000 Grenoble, France

1 Abstract

Cathode is the most crucial component of the PEMFC because the most limiting in terms of performance, durability and cost. Regarding the performance, the main losses are due to the cathode because of the negative coupling between a sluggish ORR and H⁺ and O₂ transport losses issues. Therefore, a lot of efforts were conducted on the one hand to increase the kinetic of the ORR by developing catalyst with improved activity and stability. On the other hand, attempts have been conducted to reduce mass transport losses in the cathode by tuning its nanostructure.

This paper describes a multi-step process to nano-structuring the electrocatalyst to simultaneously benefit from enhanced activity towards ORR and reduced O₂ transport limitations. Thus, a carbon-free architecture of electrodes made of organized and well-ordered and oriented PtNi nanowires and nanotubes directly embedded onto a Nafion[®] membrane was developed.

Here, the nanotubes were templated from Ni nanowires grown on an anodic aluminium oxide (AAO) template. The fabrication process was optimized to improve the quality of the nanotubes and their integration into the membrane: the process includes a thermal treatment in H₂/Ar environment and an acid leaching step as key steps to obtain the desired structure. After integrating the electrodes in a complete Membrane-Electrode Assembly (MEA), we tested the performance and durability of these nanostructures under real operating condition. We compared the results to a Pt/C conventional electrode at low Pt loading (~35 μg_{Pt}/cm²) exhibiting an ECSA close to that of PtNiNWs and PtNiNTs electrodes. Results have shown a great improvement in mass activity and stability of PtNiNTs electrodes to AST. Also, they have shown a significant sensitivity towards RH variation.



Keywords: Electrocatalyst, PEMFC, PtNi alloy, Oxygen Reduction Reaction (ORR), Electrode, Anodic Alumina Oxide, Ni Nanowires, Carbon-free electrode.

2 Introduction

Energy has always been the fulcrum of civilizations and their undeniable pillar of development. Recently, the effects of climate change are being felt even more intensely [1]. A wide range of energy sources are already known and have been used until today, such as fossil fuels, natural gas, to name a few. Recently, most of countries are aiming to vault ahead of all fossils due to their horrific effects on the environment. In the world's endless efforts to cut greenhouse gas emissions, scientist suggested possible sustainable pathways for the production of highly demanded fuels and chemicals. Hydrogen vector is coming into the spotlight, which could be used as a fuel to the polymer electrolyte membrane fuel cell (PEMFC) for electricity generation [2].

The technology of PEMFCs is a promising power source strongly motivated by its unique energy conversion efficiency of chemical energy of H_2 to electricity without emission of greenhouse gas [3]. Its commercialization is still a challenge especially due to durability and cost limitations of the catalyst [4][5]. In order to enhance their achievement on the market, it is mandatory to optimize the high costly platinum-based catalyst to increase its activity and stability. This could be reached either by tuning its composition and nanostructure, or by increasing its utilisation during operation via the reduction of mass transport limitations in the electrode, for instance thanks to innovate structures [6].

Pt-based catalysts such as Pt-Co, Pt-Cu, and Pt-Ni etc. have shown to exhibit higher oxygen reduction reaction (ORR) activity than platinum for PEMFC [7][8][9]. Commercial Pt-based (PtCo) catalysts (nanoparticles 3–5 nm) supported carbon black are considered as the current standard catalyst offering high surface areas and high specific activity. Unfortunately, they are limited by corrosion of the C and Pt dissolution/agglomeration through Electrochemical Ostwald ripening mechanism, which is reflected by a fast and significant loss of electrochemical surface area (ECSA) over time during fuel cell operation [10][11][12].

Previous studies have demonstrated the benefits of PtNi nanostructures such as nanostructured thin films (NSTF) by 3M Company [13], unsupported PtNi aerogels [14], and platinum-nickel nanowire (PtNiNW) [15]. In addition, Pt nanotubes have shown to be an interesting route to reduce Pt loading with improved stability compared to Pt/C structures [16][17]. All these nanostructures have shown very promising performance and stability for low Pt loading.

Our work focuses on reducing the amount of platinum and improving the performance and durability of membrane electrode assemblies (MEAs), aiming to reduce cost and thus encouraging the development of PEMFCs. Accordingly, we aspire to develop and control a new carbon-free architecture of the cathode, made only with vertically aligned PtNi nanotubes (PtNiNTs) supported onto a Nafion® membrane (*figure 1*).

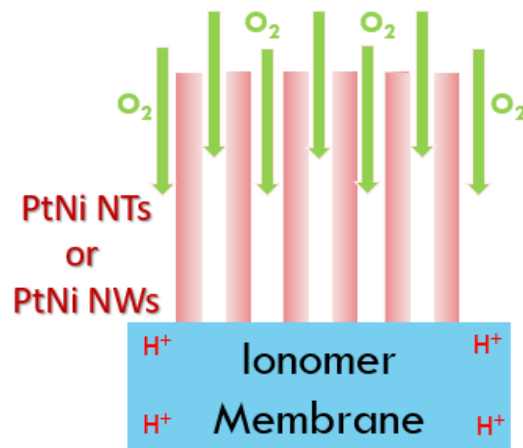


Figure 1. Scheme of the cross-section of an oriented carbon-free PtNi nanotubes (PtNiNTs) arrays transferred onto the Nafion® membrane.

We can state the differences between all these nanostructures (stated above from literature) compared to our elaborated electrodes: the oriented NSTF nanostructures [13] were supported on an organic support without carbon. Aerogels [14] exhibited larger pores' diameter and are non-oriented with tortuous morphology. For the dispersed PtNiNWs [15], the displayed a non-oriented structure as well. The latter used only the external surface of the structures.

In our study, we aimed at developing a carbon-free or support free structure, oriented and organized of PtNiNWs, and above all PtNiNTs structures in order to use both internal and external surface of the tubes. Based on this architecture, we strive to reducing the Pt loading along with the transport limitations, thanks to straight and short routes for transport of species, and optimized volumetric distribution of active sites in the absence of component without any functional properties such as a nonconductive organic support, as in NSTF.

The process is based on an electrochemistry route of Ni electrodeposition inside anodic alumina oxide (AAO) mold which is well described in literature for the growth of oriented structures.

It is followed by a step of controlled spontaneous galvanic displacement, thermal treatment and acid treatment, leading to the formation of nanotubes. The approach was first developed by Marconot et al. [18] for the fabrication of PtCu nanotubes. Based on his work combined to our original multi-step process, we have chosen PtNi as a promising catalyst which exhibited higher ORR catalytic performance [7].

Finally, the electrodes were integrated in a complete MEA in order to characterize their performance in real operating conditions, followed by Accelerated Stress Tests (AST) to study their stability.

We should point out that the optimization of PtNiNWs and PtNiNTs was described in literature for non-oriented structures but were not tested in real operating conditions in a PEMFC.

3 Experimental section

3.1 Elaboration of PtNiNTs and PtNiNWs

The fabrication process of PtNi nanotubes/nanowires is held by a succession of four steps, as displayed in *figure 2* below: **i/** the first step consists of elaborating the porous anodic aluminum oxide (AAO) as a sacrificial mold supported onto a Si wafer substrate; **ii/** The second step includes the confined growth of nickel nanowires on the silicon substrate, inside the AAO template by the pulsed electrodeposition (PED) process; **iii/** This step is followed by the galvanic displacement mechanism; **iv/** The AAO is etched in solution of NaOH resulting in self-standing PtNiNWs or PtNiNTs on silicon substrate, **v/** Finally, the last step will lead to transferring PtNi nanotubes/nanowires from the Si substrate to a Nafion[®] membrane by a hot-pressing process to test the electrochemical performance in a complete MEA.

All the steps of the PtNi nanostructure fabrications and their structure will be described in detailed in the results part.

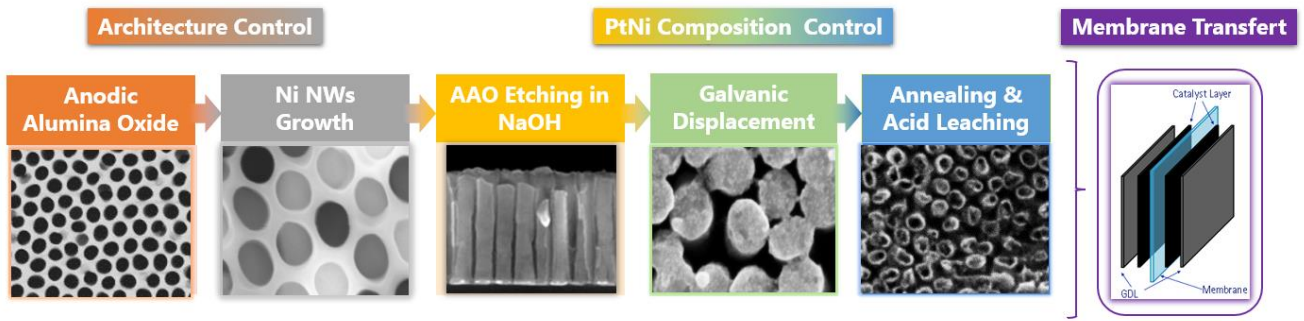


Figure 2. Methodology of the elaboration process of PtNi nanowires and nanotubes.

3.2 Microstructure

3.2.1 SEM

The morphology of the different nanostructures obtained during the process was analyzed by scanning electron microscopy SEM using a Zeiss Ultra 55 field emission gun (FEG) microscope.

3.2.2 TEM

PtNiNWs and PtNiNTs were analyzed by transmission electron microscopy (TEM). For these analyses, PtNiNWs were pulled off the Si support (or from the membrane) with a razor blade and deposited on a copper TEM grid covered with a lacey carbon film. For PtNiNTs embedded in Nafion[®] membrane, a thin section of the membrane (100 nm thick) was prepared by ultramicrotomy at room temperature using a Leica UC6 Ultramicrotome after embedding the sample in epoxy resin.

The analyses were performed using a FEI-Tecnai Osiris operating at 200 kV in the high angle annular dark field (HAADF) with scanning transmission electron microscopy (STEM) mode and equipped with a Super-X X-ray energy dispersive spectrometer (X-EDS). The quantitative analysis of Pt and Ni composition was performed using the Pt-L line and Ni-K line using Cliff-Lorimer k factors given by the EDS Bruker program.

3.2.3 X-Ray diffraction

X-ray measurements were performed in order to determine the crystallographic structure of PtNi after manufacturing. The apparatus used is a two-circles Bruker D8 diffractometer equipped with a Cu-K α source ($\lambda = 0.15406$ nm) and a LYNXEYE linear detector.

3.3 Pt loading measurement

3.3.1 UV Spectrophotometry

To quantify the actual amount of metal loaded on the carbon support, UV spectroscopy analysis measurements were carried out by using a Shimadzu 1800 UV spectrometer. The catalysts powder is initially heat treated in a ceramic oven at 600 °C for 15h so that all the components other than Pt are oxidized and vented out of the furnace. The remaining Pt catalyst powder is chemically treated to convert it to the Pt⁴⁺ ionic form, which is needed to perform the UV measurements. The treatment consists in the dilution of the Pt catalyst powder in a solution of 25vol % HNO₃ and 75 vol % HCl (Aqua Regia). The solution is completely evaporated at 100 °C into a dedicated glass system. This step is repeated twice with concentrated HCl (12 M). The obtained dry catalyst is finally diluted in HCl (1M) where the Pt⁴⁺ ions are stable. The obtained solution is analyzed to determine the catalyst concentration. A calibration of the UV spectrometer was made before each measurement by using reference samples.

3.3.2 X-Ray fluorescence

The Pt loadings were also controlled by measuring X-Ray fluorescence spectroscopy (XRF) with a Fischer-scope XDV-SDD, 50 kV, 50W X-Ray source.

3.4 Low Pt-loading Pt/C electrode fabrication

In this part, we display the fabrication process of a standard Pt/C electrode whose performance and activity will be compared to those of PtNiNWs and PtNiNTs electrodes under real PEMFC conditions. We targeted to fabricate a low Pt-loading cathode exhibiting substantially the same roughness as the cathodes made of PtNiNWs and PtNiNTs using the same Nafion[®] membrane.

The cathode-type Pt/C catalytic ink was prepared by mixing: 0.7g of catalyst powder TEC10V50E (47.2 w%Pt Tanaka[®]Pt NPs (~3 nm) deposited onto carbon support Vulcan XC72 (~40-50 nm)), 4.5 g of Nafion[®] solution D520, 20 mL of Propanol as a solvent and 20 mL Ultrapure water 18.2 MΩ.cm. The ink preparation was held in a glovebox because of safety issues related to the handling of nanopowders. The weight ratio between ionomer and carbon is 67%. After the dispersion, the ink was stirred for 72 hours with a magnetic stirrer.

Before depositing the ink onto a Poly-tetrafluoroethylene (PTFE) (250 μm) substrate, the ink was premixed in a sonicator bath beforehand for 10 minutes at room temperature to improve its homogeneity. Using the ultrasonic coating process provided by Sono-Tek[®] the ink was

sprayed onto the PTFE substrate. We quantified the Pt loading by two methods: UV–Visible Spectroscopy and X-ray Fluorescence spectroscopy (XRFS). Both techniques demonstrated a final loading of about 35-40 $\mu\text{gPt}/\text{cm}^2$.

3.5 MEA preparation

3.5.1 Half Catalyst Coated Membrane (CCM) with Pt/C electrode

The Pt/C electrode on its PTFE substrate was transferred on the Nafion[®] membrane by hot-pressing at 150°C and 2 MPa for 10 minutes. The so-obtained half Catalyst Coated Membrane (CCM) was integrated in MEA. The active area for the Pt/C electrodes is 1.8 cm² equals to that of the flow field of the cell (see **Erreur ! Source du renvoi introuvable.**).

3.5.2 Half Catalyst Coated (CCM) with PtNiNWs and PtNiNTs electrodes

We integrated these nanostructures onto a Nafion[®] HP membrane using the conventional hot-pressing process. The hot-pressing process (applied stress, time, and temperature) was optimized to transfer the nanostructures onto the membrane completely (see *figure 3*).

The hydraulic press (*Model SYNTAX*) used in assembling MEAs consists of two pedestals heated to 150°C. A loading force was imposed on the upper pedestal to apply stress of 1 MPa for 13 minutes. GDLs and gaskets are used to compensate for eventual unevenness or misalignment on the pedestal surfaces.

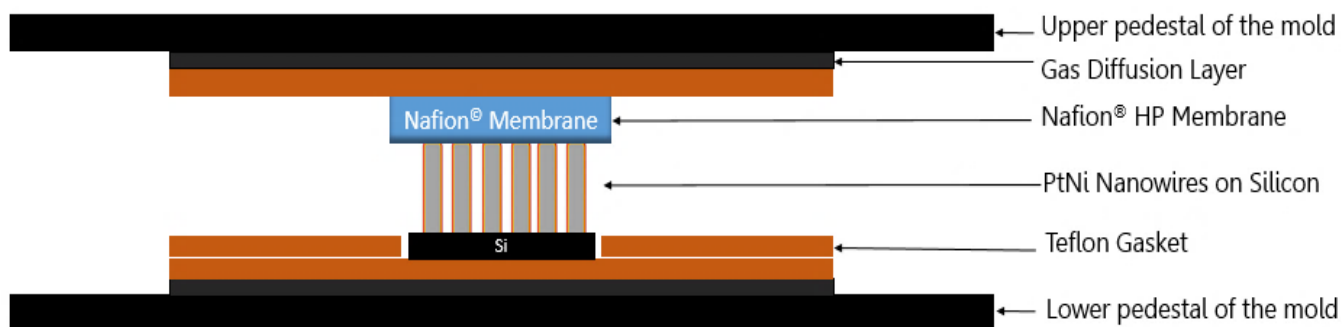


Figure 3. Schematic illustration of the hot-pressing process used to integrate the supported PtNiNWs and PtNiNTs electrodes on the Nafion[®] HP membrane.

For both NWs and NTs, once the pressing process is over, we recover the membrane gently with silicon substrate stuck into it. The latter is washed in sulfuric acid H₂SO₄ 0.5 M for three reasons: **i/** facile removal of silicon substrate from the ionomer membrane without tearing it up, **ii/** nickel leaching, and **iii/** membrane re-acidifying. The active area for the PtNiNWs and PtNiNTs electrodes at the cathode is about 0.3 cm² and 0.16 cm², respectively. The active area

of the anode is always 1.8 cm². The active area of the GDL is 1.8 cm² for both anode and cathode.

3.5.3 MEA from half CCM

A Gas Diffusion Layer (GDL) Sigracet 24BC from SGL (235 μm) was used at the cathode in contact with either the Pt/C, the PtNiNWs or the PtNiNTs electrodes. In-house made Gas Diffusion Electrode (GDE) as an anode (Pt/C TTK 50 %wt on Vulcan carbon, 0.1 mg/cm² on GDL Sigracet 24BC from SGL) was chosen for the anode side. PTFE (150 μm) and Poly(ethylene-naphtalate) (PEN) wedges (25 μm) respectively used as gaskets and as mechanical reinforcements, were placed between the monopolar plates and the MEA, to ensure a good gas sealing with a compression of the GDL of 25%, leaving only the active area to exposed to gases. MEAs were assembled into differential cell following the same aforementioned protocol assembly than for the Pt/C based electrode (see *Support Information SI 1* for further details).

3.6 Single cell and operating conditions

The MEA were placed in differential fuel cell that allows studying under homogeneous and well-defined conditions for in-depth electrochemical characterization in representative operating conditions.

3.6.1 Single cell

The fabricated MEA was tested under homogeneous and well-defined conditions of relative humidity (RH), cell temperature, and gas flow as demonstrated by *Fontana et al.* [19]. The active area of the flow field is 1.8 cm². Reduced dimensions and high stoichiometric ratios characterize this type of cell. A differential cell's purpose is not to be operated as a technical device but to emulate the local conditions of a larger device and study the effect of different operating parameters at a local scale without the disturbance of along the channel effects [20]. Graphite flow fields with multi-straight and parallel channels are used on both the anode and the cathode side.

3.6.2 Operating conditions

The cell was mounted in an in-house test stand that allows a precise control of the conditions protocol during operation, as summarized in *table 1* below. The cell temperature is controlled via circulation of hot water on both anode and cathode plates. Thermocouples placed very

closed to the active area allow to check that the difference in temperature between the anode and cathode plates is negligible, namely less than 0.2°C. During the test, the active gases used are Air or Oxygen at the cathode and Hydrogen at the anode.

	Experimental values			
Operating conditions	Anode		Cathode	
Temperature [°C]	80			
Gas	H₂		O₂ or Air	
Relative Humidity [%]	80	100	80	100
Absolute Pressure P_{tot} [bar]	1.38	1.5	1.38	1.5
Flow rates [Nl/h]	35			

Table 1. Operating conditions for testing differential cells.

3.6.3 Conditioning

Prior to testing, the MEA was pre-conditioned (break-in step) via voltage cycling using a lab-developed protocol as referred in *Support Information SI 2*. The MEA conditioning was carried out in H₂/O₂ at 1.5 bar and relative humidity of 100% (fully humidified gases) at 80°C for several hours to reach the maximum performance of the cell.

3.7 Electrochemical characterisations

3.7.1 Electrochemical surface area measurement

Cyclic Voltammetry (CV) measurements are performed in order to determine the specific electrochemical surface area. It refers to the catalyst's surface area in contact with the electrolyte, accessible to protons from the membrane, and electrically connected to the current collector. The experiment was carried out at 80°C with a *Biologic*[®] potentiostat monitored by the *EC-Lab* program, with a fully humidified flow of H₂ and N₂ at the electrode that is used as the anode and at the cathode in fuel cell operation, respectively.

The roughness is calculated from hydrogen desorption coulometry after underpotential deposition (H_{UPD}) and determined according to the following expression (*equation 1*). Further details are expressed in *Support Information SI 3*.

$$\text{Roughness} = \frac{Q_{des}}{0.21 \times S_{electrode}}$$

Equation 1

where: - $S_{electrode}$ refers to the real geometric surface area of the electrode in cm^2_{geo} ;
 -Roughness: in $\text{cm}^2_{\text{Pt}}/\text{cm}^2_{\text{geo}}$;
 - Q_{des} : charge obtained by integrating the dashed blue area in C.

3.7.2 Ohmic resistance measurements

The ohmic resistance as a function of RH was measured thanks to impedance measurement at different relative humidity under H_2/N_2 , as for ECSA measurements. Potentiostatic Electrochemical Impedance Spectroscopy (PEIS) measurements were held from 200kHz to 100Hz at $0.4V_{\text{RHE}}$, where no adsorption/desorption reactions are observed in this region, as confirmed by the absence of redox peaks in the CV. We performed measurements in a potentiostatic mode, where a perturbation around a fixed value of voltage (10mV) is applied. Simultaneously, its current response is measured (the amplitude of the applied signal should be small to be in the linear regime). Considering the PEIS experiments carried out in this work and the very thin CL used in cathode, we could not dissociate the losses related to protons transport through the active layer. Thus, we will settle for the high-frequency resistance (the value of impedance for which the imaginary part is equal to zero at high frequency) to quantify the ohmic resistance of the cell R_{ohmic} .

We will settle for the high-frequency resistance (the value of impedance for which the imaginary part is equal to zero at high frequency) determined by PEIS at $0.65V_{\text{RHE}}$ to correcting the polarization curves from the ohmic drop, and to compare the performance accurately (refer to *Support Information SI 2* for further details).

$$E_{\text{cell},iR\text{-free}} = E_{\text{measured}} + R_{\text{ohm}} \cdot j$$

Equation 2

Where $E_{\text{cell},iR\text{-free}}$ is the ohmically-corrected potential, E_{measured} is the measured cell potential, R_{ohm} is the ohmic resistance, and the j is the current density.

4 Results

4.1 PtNiNTs and PtNiNWs fabrication and structure

4.1.1 Anodic Alumina Oxide (AAO) fabrication

In order to obtain straight aligned and organized Pt-Ni nanowires and nanotubes, we leaned out to use tuned mold-based templates made of aluminum oxide. To that end, several steps are required to obtain the desired structure of the anodic alumina. The first step will consist of the manufacturing of the nanoporous alumina template with vertically oriented organized pores. Its design will govern the final organization of the electrode. Tuning the parameters of anodization, the achieved template will be used as a mold for the growth of the nickel nanowires, which are considered precursors for the PtNi nanotubes.

Here, we report the process of double anodization after optimization to obtain nanostructures with the desired dimensions, ranging from 50 to 150 nm in pores' diameter and 0.1 to 1 μm in depth. A detailed fabrication process was described exhaustively elsewhere [21][22][23][24][25][26][27][28][29]. The anodization process follows a multi-step procedure to obtain the desired geometry of nanoporous AAO templates:

- i.** Formation of massive alumina layer at the beginning of the process;
- ii.** Nanopores initiation and growth of parallel nanochannels;
- iii.** Wet etching process in an acidic solution, which leads to the formation of hollow and ordered nanocells.

By tuning the anodization parameters, which directly impact the kinetics of the pores' formation, we tend to control the thickness of AAO, which would be the final length and diameter of the nanowires when grown onto the matrix. The first anodization has two main interests: **i/** removing a controlled thickness of aluminum and **ii/** obtaining a pre-patterned aluminum surface after the wet etching. The latter, performed in the right conditions, would predict the final pores' size (*i.e.*, porosity and density).

In our experiment, we used the mild double anodization process as described by Masuda et al. [29] as shown in *figure 4*. It is used for highly ordered and homogeneous templates at a slow rate growth of nanochannels. It exhibits low current density at a fixed voltage (*i.e.*, low anodizing potential) and a low concentration of acidic solution.

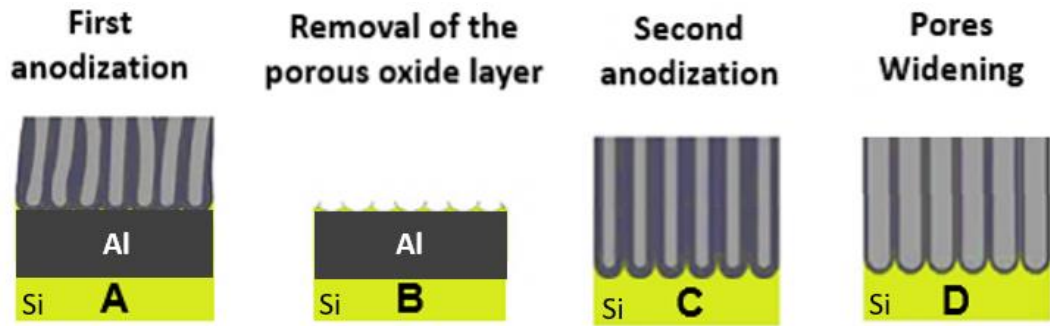


Figure 4. Scheme of the two-step anodization process for the fabrication of a nanoporous alumina template, where the green side refers to the Silicon substrate and the black bulk to aluminum layer. **A)** formation of irregular AAO pores after 1st anodization, **B)** first AAO etching in orthophosphoric acid leaving nanobowls on the aluminum surface, **C)** regular pores formation after 2nd anodization and **D)** pores widening process in orthophosphoric acid.

The template was made on a highly doped p-type silicon wafer (very low resistivity ρ ($\rho < 0.01 \Omega \cdot \text{cm}$)) by electrochemical oxidation of a 1-5 μm aluminum thin layer deposited through physical vapor deposition PVD sputtering in an evaporation set-up under a vacuum of approximately 10^{-7} mbar. The mirror-like aluminum surface indicates the surface's low roughness. Also, post-deposition annealing was performed at 300°C would improve the adhesion between the aluminum film and silicon substrate and increase the Al grain size [30][31].

Aluminum anodization was carried out in a home-made PVC (Polyvinyl Chloride) electrochemical cell, chemically resistant to the acidic electrolyte, as shown in an apparatus in *figure 5*. The detailed process of double anodization is well detailed in *Supporting Information SI 4*.

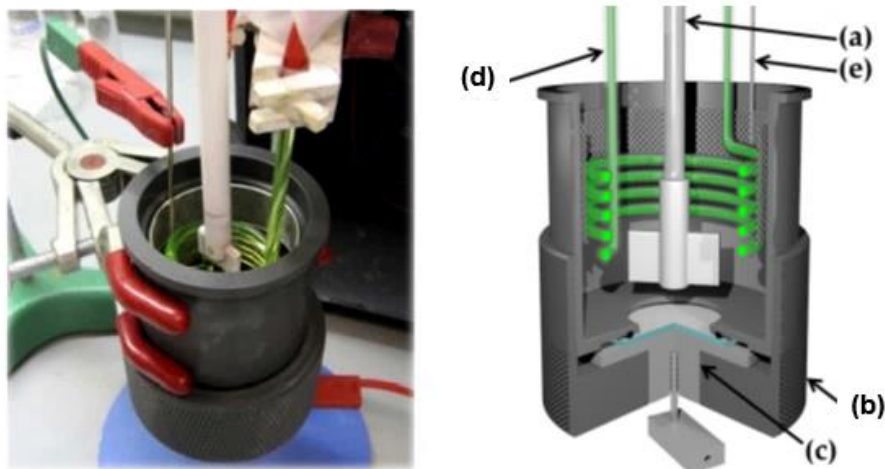


Figure 5. Electrochemical cell setup used for anodizing aluminum on p-type silicon substrate (Left picture) and 3D model of the PVC cell (right picture) composed of: **a)** Stirrer, **b)** PVC core, **c)** Metal cap that ensures electrical contact and mechanical cohesion between the cell and the sample (electrode), **d)** Flowing cooling Liquid system to adjust the temperature of the electrolyte, **e)** Cylindrical platinum gauze as counter-electrode.

As evidenced in the literature, the etching rate is dependent on the chemical composition of the pore wall oxide of AAO [32]. More details about the evolution of pore diameter (D_p) are referred in *Supporting Information SI 5*.

Figure 6 below exhibits the AAO template obtained by double-anodization process with almost uniform pores' size throughout this work

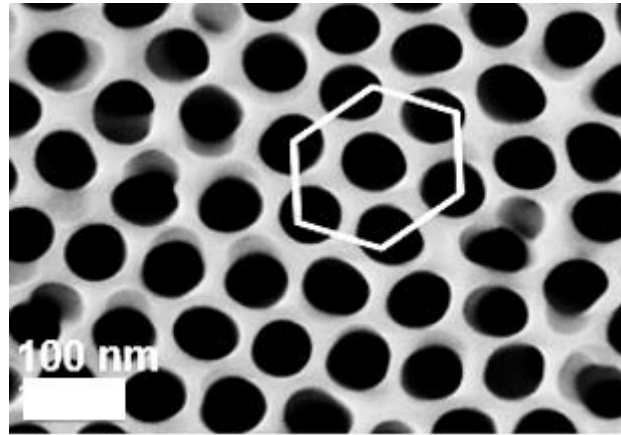


Figure 6. A scanning electron microscope (SEM) image of the nanoporous anodic aluminum oxide fabricated during this work through the double-step anodization process in 3%wt oxalic acid, under potentiostatic regime, with an applied voltage of 34 V at 23°C.

After the fabrication of anodic aluminum oxide by a double-step anodization process, a substantial annealing step is required before embarking on NiNWs growth. Thermal treatment of AAO samples has been carried out inside a resistance furnace (*i.e.*, by Joule effect) with a homogenous and controlled circulation of gaseous Nitrogen at 100 mbar to get rid of all possible generated gases. The annealing temperature should remain below $\sim 1050^\circ\text{C}$ to avoid alumina phase transformation (*i.e.*, crystallization) to γ -alumina, which is resistant to chemical etching [33]. Also, since we are using an Al/Si substrate, annealing temperature should not reach the aluminum melting point ($\sim 650^\circ\text{C}$) to create AlSi alloy during thermal treatment. For such conditions, the annealing temperature is therefore chosen to be 450°C . This step is mandatory and provides a framework onto which we can not only reduce organic contaminants and anions from the electrolyte (oxalate and phosphate anions) incorporated in nanoporous alumina [34] but also to get rid of water molecules which can, thereafter, react with vapor HF during deoxidation step.

4.1.2 Nickel nanowires (NiNWs) confined growth inside AAO

Nanoporous aluminum oxide was found to be ideal for the growth of dense nanowire arrays, providing ordered, parallel, and uniform pore channels with a high aspect ratio and mechanical support to fragile nanowires [35][36].

In this study, we have chosen the pulsed electrochemical deposition (PED) in an aqueous solution for NiNWs growth. PED's main advantages, which allowed better control over the deposition parameters and the length of NiNWs, rely on its flexibility to adjust the amplitude and duration of the voltage pulses. It offers the possibility of introducing a delay pulse to refresh the metallic ions concentration at the deposition interface, promoting uniform nanowire growth [36].

Prior to electrodeposition, the electrical contact at the bottom of the pores is not homogeneously ensured due to the silicon electrochemical oxide formed at the end of anodization. A silicon deoxidization step by vapor HF was added to the process to overcome this issue (*Supporting Information SI 6*). *Figure 7* below shows the homogeneous deposition of NiNWs inside the AAO template.

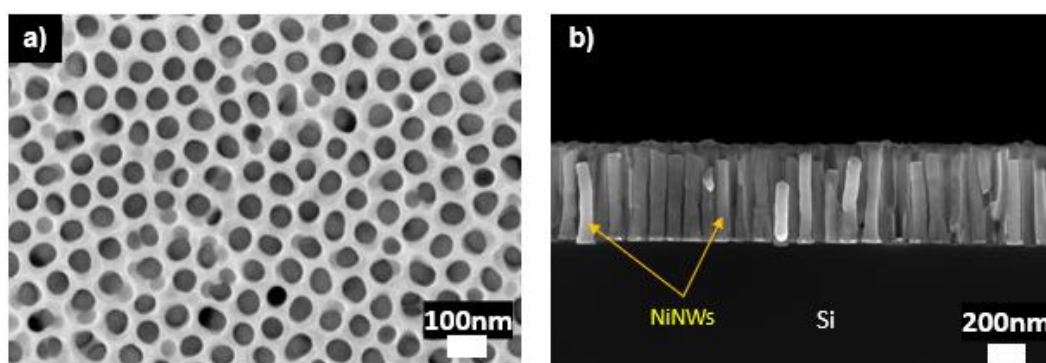


Figure 7. SEM micrographs of top view **a)** homogeneous NiNWs inside alumina template and a cross-sectional view **b)** of NiNWs growth inside anodic aluminum oxide, with HF deoxidation step, which is mandatory to obtain homogeneous NiNWs deposit.

Nickel nanowires were grown in AAO mold, using the Watts bath solution: a mixture of 300 g/L $\text{NiSO}_4 \cdot 6\text{H}_2\text{O}$, 45 g/L $\text{NiCl}_2 \cdot 6\text{H}_2\text{O}$, and 45 g/L H_3BO_3 as a buffer [37][38] (see *Supporting Information SI 7-8*).

The magnetic stir bar was put in the container containing the solution to be stirred at 35-40°C. The pH of the solution was measured to be 4. It has been suggested that boric acid stabilizes the pH and enhances metal deposition.

To perform Ni PED, the sample is maintained inside an adequate homemade electrochemical cell (same electrochemical cell as the one used for aluminum anodization) where the electrical contact between the electrolyte and the working electrode is ensured at the bottom of nanopores on the conductive silicon substrate.

Finally, the electrodeposited nickel into porous alumina templates created ordered nanowires as depicted in *figure 8-a-b and c*). Pulsed currents helped improve the deposits' quality by

smoothing surface may be due to Ni oxidation, and allowing good adherence to the substrate). The deposition time was varied to control the length of the nanowires. The slight difference in NiNWs length in *figure 8-c*) is attributed to the aluminum deposition's surface unevenness on silicon.

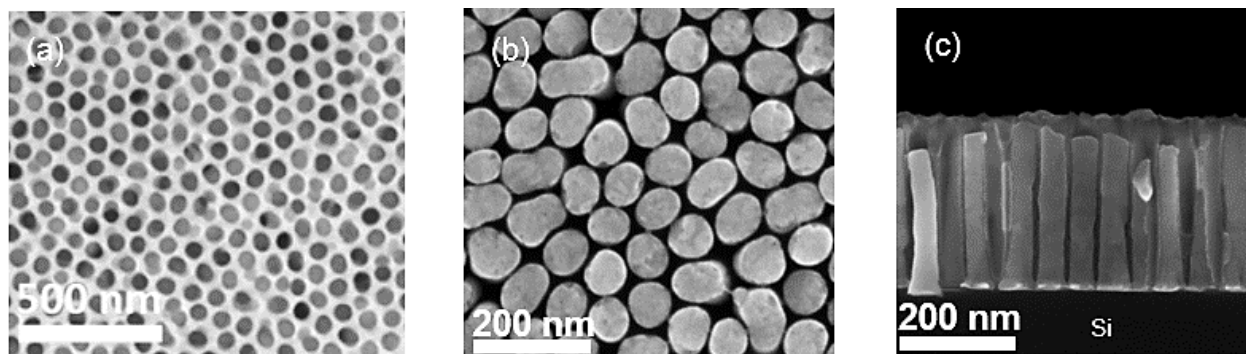


Figure 8. Scanning Electron Microscopy (SEM) observations of Nickel nanowires grown inside porous anodic alumina template (PAAT), **a)** SEM top view of Nickel nanowires before alumina etching, **b)** SEM Top view of Nickel nanowires after alumina etching, and **c)** SEM cross-sectional view of Nickel nanowires after alumina etching.

4.1.3 PtNiNWs and PtNiNTs fabrication from NiNWs as a sacrificial template

4.1.3.1 PtNiNWs fabrication

This part describes the complete protocol followed in this work to synthesize PtNi nanowires with the galvanic displacement process (according to the reactions below), accompanied by post-treatments: heat treatment and acid leaching process.



For this purpose, the nickel nanowires were exposed to Pt salt solution in a non-confined environment, where the AAO was completely etched in a heated solution of 5%wt orthophosphoric acid at 35°C.

PtNiNWs (*figure 9*) were obtained after 8 minutes GD reaction at 35°C in Potassium tetrachloroplatinate (K_2PtCl_4) solution with HCl 0.05 M. A SEM-EDX quantitative analysis on the resulting NWs have shown an atomic ratio Pt/Ni = 3 (Pt_3Ni), displayed in *figure S17* and *S18*, alongside XRD measurements as demonstrated in *figure S19* in *Support Information SI 9*.

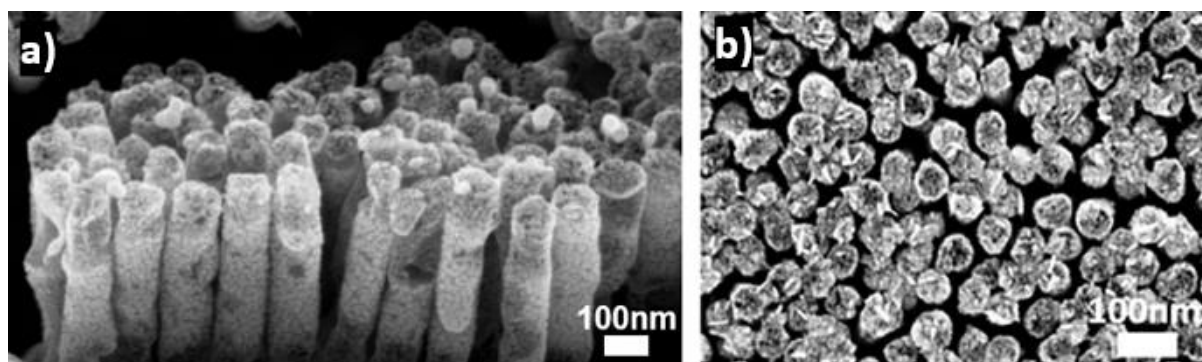


Figure 9. SEM cross section view (a) and top-view (b) structural characterization of PtNiNWs after exposing NiNWs/Si to a K_2PtCl_4 solution in 0.05 M HCl at 35°C for 8 minutes.

Figure 10 below summarizes the reproducible fabrication process of PtNiNWs as follows:

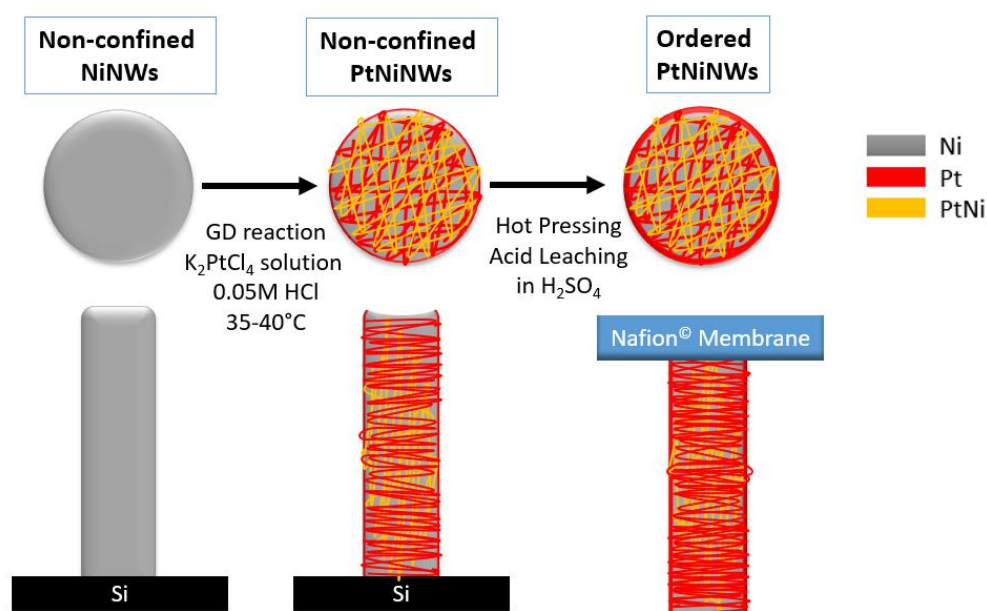


Figure 10. Schematic illustration of various stages involved in fabricating PtNi nanowires.

4.1.3.2 PtNiNTs fabrication

On the other hand, the elaboration of PtNiNTs has followed a different process. Firstly, the self-standing NiNWs on Si were dipped in a Potassium tetrachloroplatinat (K_2PtCl_4) solution without HCl at 80°C for 90 minutes (details were given in *Support Information SI 9 – PtNiNTs Fabrication*).

After several sets of experiments regarding the temperature's effect, we noticed that temperature has a significant effect on the rate of the reaction. Once the experiment is over, the sample was rinsed in distilled water. The PtNiNWs were analyzed by TEM (*figure 11*). The Ni

and Pt X-EDS elemental maps (*figure 11*) reveal that the reaction had led to the deposit of a thin layer containing Pt of $\sim 4\text{-}5$ nm onto the Ni nanowires.

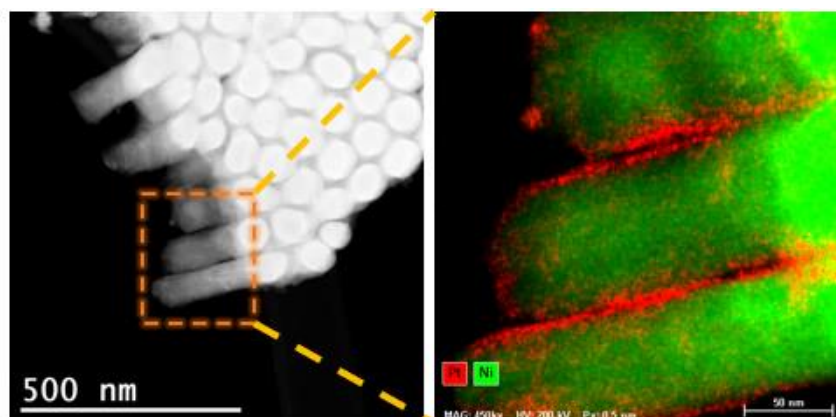


Figure 11. HAADF/STEM image and the associated Pt and Ni X-EDS elemental maps for PtNiNWs (intermediate step before the formation of PtNiNTs) Pt species are in red, and Ni species are in green.

A higher magnification HAADF/STEM image coupled X-EDS analyses of a single PtNiNWs was performed (*figure 12*). These analyses clearly reveal an oxide shell serving as a Ni protective shell from the deposition of Pt cations during the reaction, which might inhibit the GD reaction to take place. From this analysis, we can conclude that PtCl_4 is likely to be deposited instead of pure Pt as demonstrated by the presence of Cl.

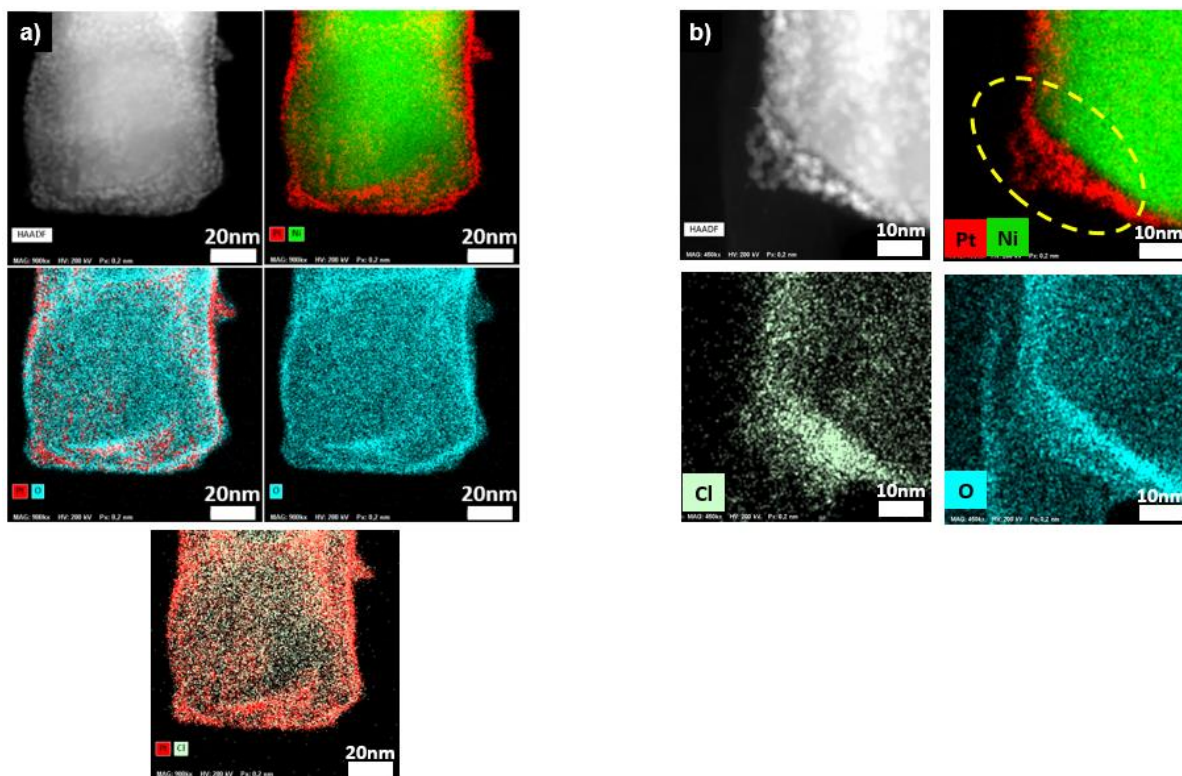


Figure 12. a) HAADF/STEM images and the associated Pt, Ni, O and Cl X-EDS elemental maps of the PtNiNWs as-synthesized (without HCl addition), obtained after galvanic displacement in K_2PtCl_4 at 80°C . Red mapping refers to Pt, Green mapping refers to Nickel, Light-green mapping refers to

Chlorine and Blue mapping refers to Oxygen. **b)** Higher magnification HAADF/STEM image and associated X-EDS analysis of the same sample.

The sample was further characterized by X-ray diffraction (XRD) in order to determine the crystalline structure of the metal phases. Concerning XRD on these PtNiNWs, measurements exhibit two peaks related to the face-centered cubic Nickel, with angular positions 44.5° and 51.8° , corresponding respectively to Ni(111) and Ni(200) crystalline planes. In addition, a very small peak is detected at 39.8° , which might refer to (111) peak of pure Pt (see *figure S22* in *Support Information SI 9*).

The resulted PtNiNWs were annealed in a H_2/Ar atmosphere in an attempt to improve the incorporation of Ni into the Pt phase. Based on the previous works of *S. M. Alia et al.* [20][39], and *C. Fan et al.* [40], the thermal treatment under H_2/Ar atmosphere and the acid leaching is playing a pivotal role in the formation of a porous structure of PtNi nanowires.

Annealing was conducted using a thermal quartz tube furnace under H_2/Ar 5% atmosphere. A complete purge of the furnace was set for 2 hours. The increased rate of temperature in the furnace is $10^\circ C/min$ until reaching the desired temperature. Once the annealing process ends, the temperature decreases until it reaches room temperature. A schematic diagram of the annealing process of PtNiNWs in the RTA system is shown in *figure 13*.

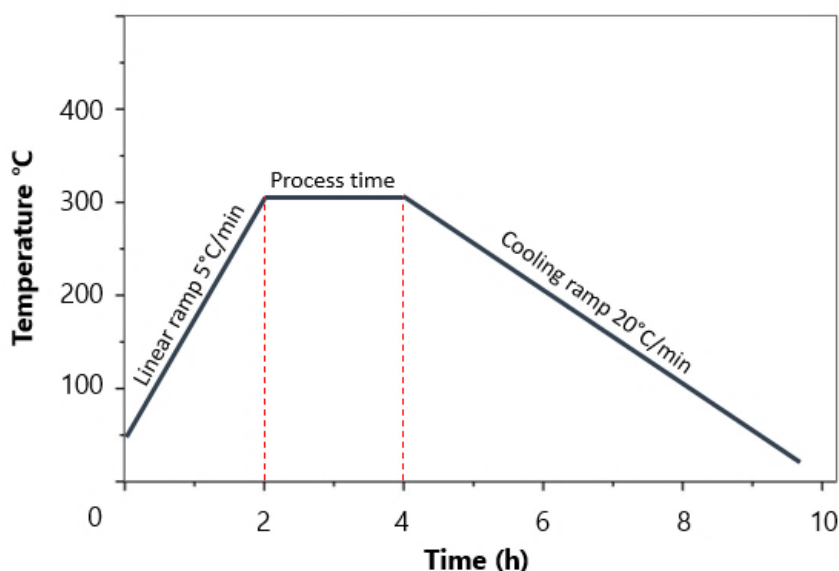


Figure 13. A schematic diagram of the annealing process in RTA (Rapid Thermal Annealing) temperature.

The next step consists of transferring the annealed PtNiNWs onto the Nafion[®] HP membrane (thickness: $22\ \mu m$) by the hot-pressing process at $150^\circ C$, 1MPa for 12 minutes.

Once the PtNi nanowires were entirely transferred to the ionomer membrane, the latter is then immersed in the 0.5M sulfuric acid solution for dealloying (acid leaching process), re-acidifying the membrane, and helps to tear off gently the polymer from the silicon substrate. For the acid leaching (AL), however, the goal was not to remove all the nickel but the soluble nickel of the PtNiNWs that was not alloyed to the Pt. Finally, after AL, we obtain a forest of well-organized PtNiNTs on the membrane as can be seen in *figure 14*.

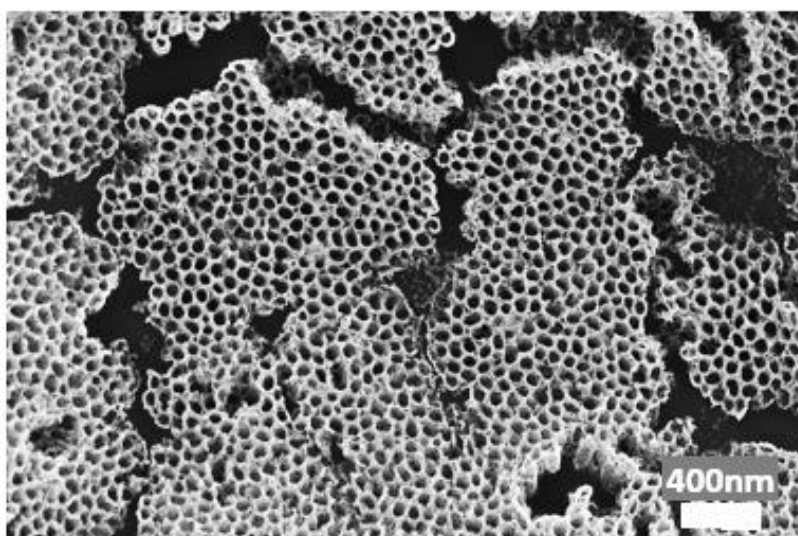


Figure 14. SEM image of top view of PtNi nanotubes transferred to Nafion[®] membrane after acid leaching.

The synthesized PtNiNTs were analyzed by TEM and X-EDS (*figure 15*) The HAADF/STEM images reveal the formation of a nanotube porous structure (*figure 15-a*). A part of these nanotubes are well integrated onto the Nafion[®] membrane that can be clearly imaged by the F elemental map.

The Pt and Ni X-EDS elemental maps show that the chemical composition of the nanotubes is not homogeneous on their length (*figure 15-a and b*); the upper part of the nanotube that is not embedded in the membrane has a higher Pt content (92 at% Pt and 8 at.% Ni) than the lower part embedded in the membrane (73.5 at% Pt and 26.5 at.% Ni). These analyses indicate that the acid leaching occurred more at the nanotube region not embedded on the membrane and spread less toward the embedded area onto the membrane.

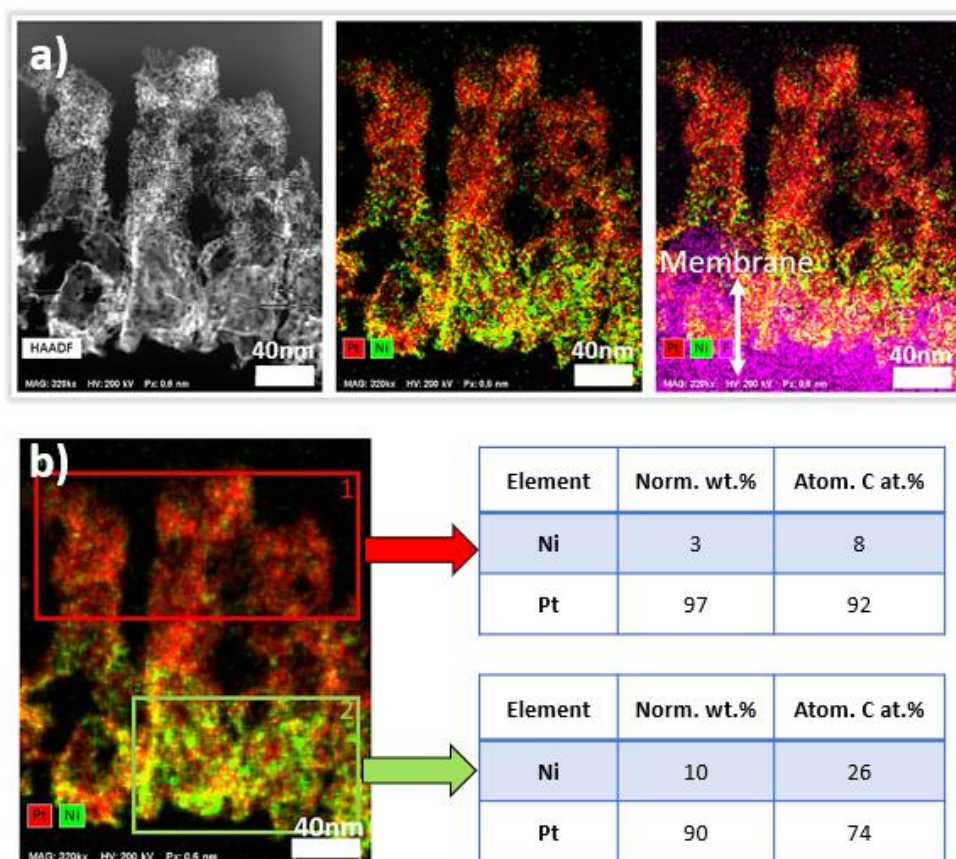


Figure 15. a) HAADF-TEM image and associated X-EDS Pt, Ni and F elemental maps of the porous PtNiNTs embedded onto the Nafion® membrane. b) The corresponding Pt and Ni elemental maps showing gradient of composition and the Ni and Pt composition quantified in the two different areas.

XRD experiments were performed on this sample of PtNiNTs embedded onto the Nafion® membrane. The obtained pattern (*figure S24* from *Support Information SI 9*) revealed a very low signal at 39.8° matching with the (111) peak of pure Pt, indicating a low content of Pt in the sample.

To sum up, several steps were involved in the formation of PtNiNTs (*figure 16*).

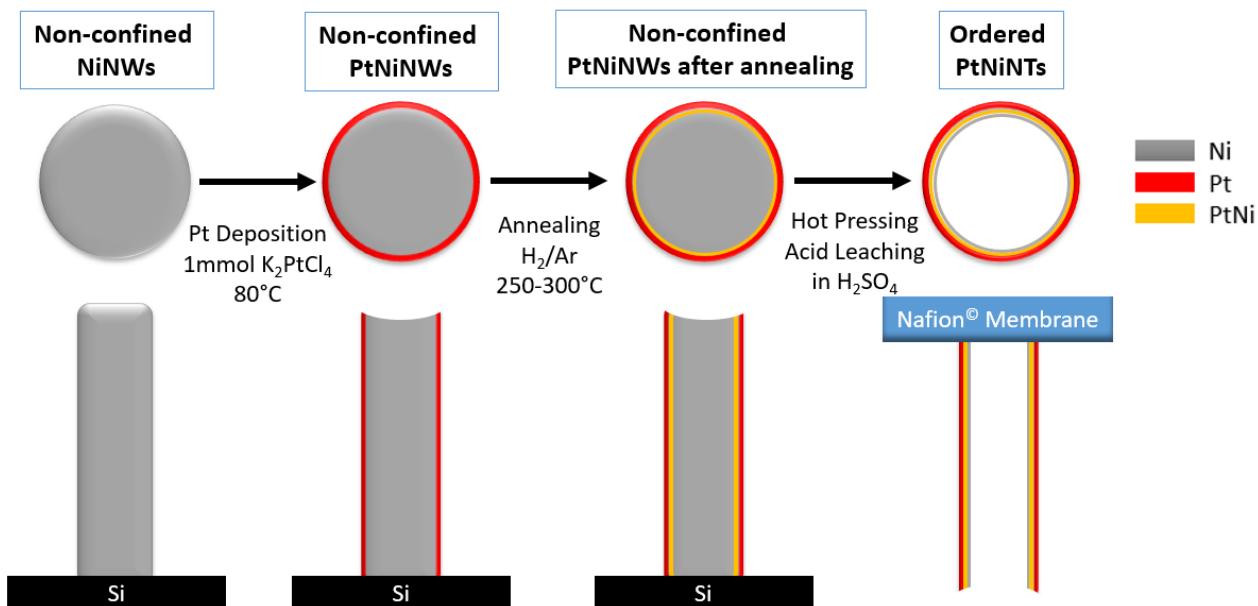


Figure 16. A schematic illustration of the complete process of the steps involved in the elaboration PtNi nanotubes.

In *Supporting Information (SI 9)* section, we stated in detail the experimental process alongside TEM and XRD analysis.

The synthesized electrodes will further be transferred to MEA then evaluated and applied as the cathode catalysts for a single differential cell.

The SEM images in *figure 17* show the cathode's final self-supported nanostructures after the complete integration of PtNiNWs and PtNiNTs on the Nafion[®] HP membrane.

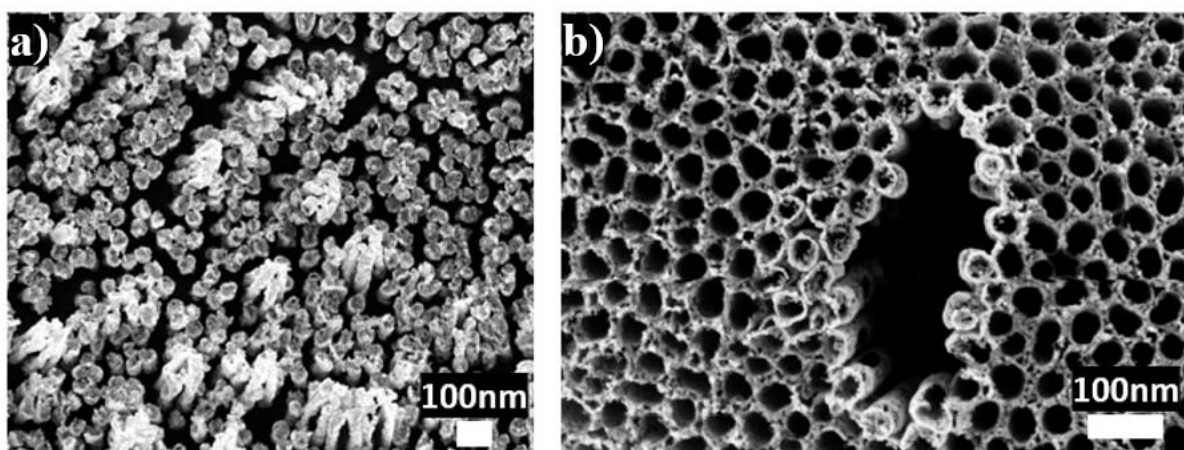


Figure 17. SEM images of top-view of the sample a) PtNiNWs and b) PtNiNTs array structures transferred onto the Nafion[®] membrane by the hot-pressing process.

We designed the PtNi nanostructure to reach a Pt loading of about 0.1 mg/cm² for the PtNi nanotubes, with a diameter of 50 nm, which defined the final length of the nanostructures being

about 250-300 nm. We chose this dimension so as the inner diameter of the tubes is around 30 to 40 nm that corresponds roughly of the size of the secondary pores in the conventional Pt/C nanostructure.

Pt loading of PtNiNWs and PtNiNTs electrodes is respectively 100 and 15 $\mu\text{g}/\text{cm}^2$. Thus, the final loading of the nanostructure is far lower than calculated considering bulk structures. This means that the PtNi nanowires and the walls of the PtNi nanotubes are porous and are made of PtNi alloy nanoparticles, as shown on SEM and TEM images.

The Pt loading of the PtNiNWs and PtNiNTs can be tuned by changing the diameter, length, of the nanostructure, the composition of the PtNi. However, these parameters are not independent and changing the dimensions of the nanostructure will induce modification of the size and composition of the PtNi nanoparticles that make the tubes.

The synthesized electrodes are transferred to the membrane to obtain an MEA, and then evaluated as the cathode in single differential cell tests.

4.2 PtNiNWs and PtNiNTs performance and stability vs conventional Pt/C electrode

This part will depict the electrochemical characterizations in relevant operating conditions of the MEA made of conventional Pt/C catalyst at low Pt loading, PtNiNWs, and PtNiNTs as cathodes. Studies have been completed and intended to quantify the performance compared with standard Pt/C electrodes and quantify the activity and transport limitations in different operating conditions, especially in dry or wet conditions. The robustness towards the accelerated stress test has also been evaluated.

4.2.1 Electrochemical surface area

In our experiment performed on the Pt/C, PtNiNWs and PtNiNTs electrodes whose Pt loading is respectively 35, 100 and 15 $\mu\text{g}/\text{cm}^2$. The roughness reads about 7.3 $\text{cm}^2_{\text{Pt}}/\text{cm}^2_{\text{geo}}$, 6 $\text{cm}^2_{\text{Pt}}/\text{cm}^2_{\text{geo}}$ and 3.7 $\text{cm}^2_{\text{Pt}}/\text{cm}^2_{\text{geo}}$, respectively, as displayed in *figure 18 (a-c)* below.

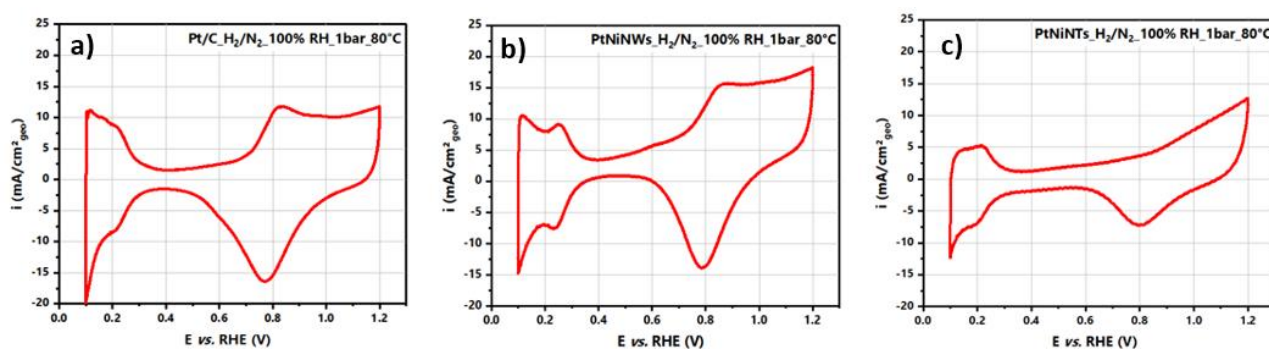


Figure 18. Cyclic voltammograms (CV) of **a)** Pt/C, **b)** PtNiNWs and **c)** PtNiNTs, recorded in fully humidified H_2/N_2 gas flow from $0.1 V_{RHE}$ to $1.2 V_{RHE}$ at $80^\circ C$ with a sweep rate of $200 mV/s$.

The difference in the shape between the CV obtained with PtNiNWs and PtNiNTs on *figures 18b* and *18c* respectively indicate that the nanostructure of the PtNi nanoparticles, that is to say size, shape and crystalline orientations most probably differ between the two electrodes.

4.2.2 MEA performance

In this work, and after conditioning, we have tested the fuel cell's performance under wet H_2/O_2 gas flow at different relative humidity values at $80^\circ C$, by keeping the partial pressure of O_2 at the inlet constant.

We compared performance of each MEA at different relative humidity. Polarization curves for Pt/C, PtNiNWs and PtNiNTs were recorded at $80^\circ C$ in H_2/O_2 and H_2/Air at 80% RH and 100%RH, at a total pressure of 1,5 bar and 1,38 bar, respectively. The ohmic resistance decreases as RH increases thanks to the enhancement of proton conductivity of the ionomer upon hydration.

Thus, the polarization curves were corrected from the derived ohmic resistances from EIS measurements as depicted in *figure 19* below. Therefore, the only difference in performance is due to the operation of the electrode that depends on the activity of the catalyst and on its utilization related to the O_2 and H^+ transport limitations.

Comparison under O_2 :

From the polarization curves, we notice that the RH affects the PtNiNWs and PtNiNTs electrodes' performance, while the Pt/C electrode is much less impacted. The performance of the PtNiNWs decreases significantly from 100% to 80% RH at low current density, below $0.8 A/cm^2$. This is ascribed to a decrease in the use of the catalyst surface area due to H^+ transport limitations. Indeed, there is no ionomer on the ~ 250 nm long PtNiNWs. At 100%RH, one can

expect proton transport on the surface of the hydrated catalyst (NWs/NTs) up the end of the reduced length nanostructure, that-is-to-say close to the GDL, even in the absence of ionomer thanks to proton transport phenomenon similar to that suspected to rule the operation of NSTF, as described by *Eikerling* [41], or *Zenyuk* [42]. In the absence of ionomer, the amount of water content on the surface of the catalyst is most probably significantly reduced at 80%RH, if exists. Thus, the proton transfer must be drastically limited in this condition resulting in electrochemical reaction restricted to the area very close to the membrane surface where there is ionomer, namely on a much lower surface than at 100%RH.

At higher current density, above 0.8 A/cm², the increase in water production probably leads to local water condensation in or close to the catalyst layer even at 80%RH in the channel. The proton conduction path would then be restored allowing reaching better performance at 80% RH than at 100% RH, probably because of the lower O₂ transport limitations in GDL less saturated with liquid water. This phenomenon is not observed in the Pt/C based electrodes that contain ionomer. Regarding the PtNiNTs electrodes, that is also free of ionomer, if a decrease in voltage is observed from 100% to 80% RH for current density lower than 0.2 A/cm², the performance is much better at 80% RH than at 100% RH above 0.2 A/cm². This electrode seems to very sensitive to flooding compared to PtNiNWs when reaching high relative humidity but is able to keep some hydration at low RH maybe thanks to capillary condensation in the porous wall of the tubes or in the inner of the tubes. When comparing the performance of the electrodes at 100% RH, one can see that the PtNiNWs electrodes perform better at low current density than the two others, but its performance decreases drastically above 0.6 A/cm². The best performing in this condition is the Pt/C electrode, while the PtNiNTs shows the lowest performance. Similar performance with low loaded Pt/C electrode can be found in the literature, as demonstrated by *Liu et al.* who reported better performance with 20wt% Pt/C catalyst from JM with a loading of 50 μg/cm² under pure O₂ **Erreur ! Source du renvoi introuvable.** With such Pt loading, and roughness, the performance dramatically decreases in air (*Figure 20*).

At 80%RH, the PtNiNTs electrode has the lowest voltage below 0.2 A/cm² but gives the best performance above 0.8 A/cm², while the PtNiNWs electrode is the least performing at high current density. It shows here how sensitive to RH these nanostructures are, which has also been reported for NSTF [13]. These results also emphasize the potential interest of PtNiNWs or PtNiNTs electrodes depending on RH. More results of the effect of RH at the Anode and Cathode respectively are described in the *supplementary information*. The best performance

was achieved at 100% RH for Pt/C, and PtNiNWs, and 80%-100% RH (anode and cathode, respectively) for PtNiNTs.

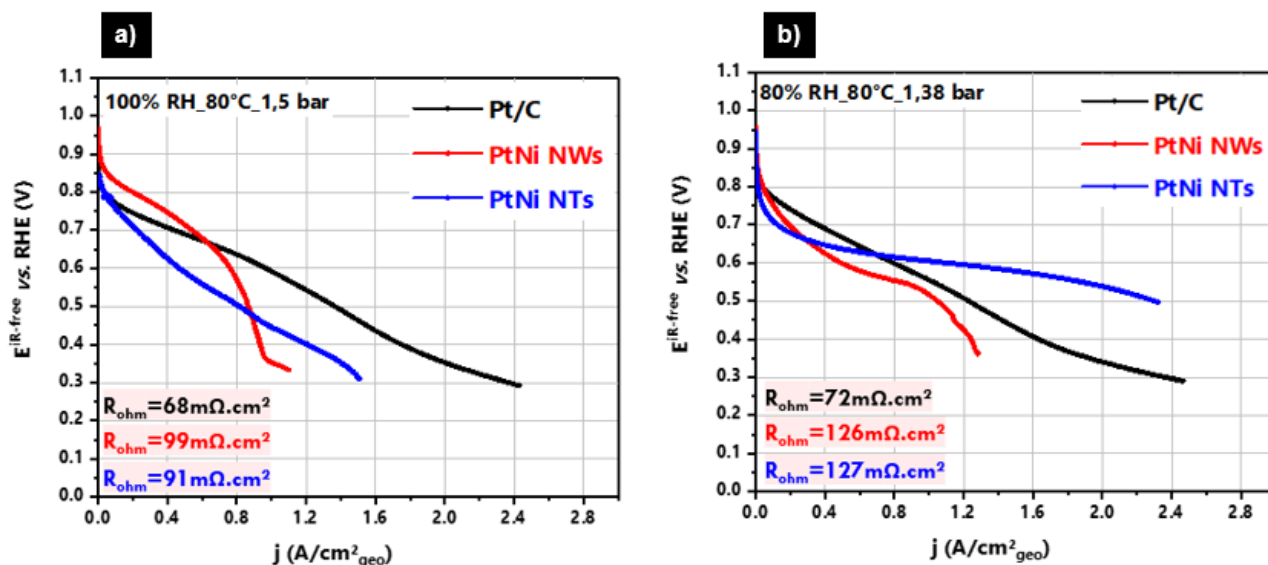


Figure 19. Comparison of fuel cell's ohmically-corrected polarization curves of Pt/C, PtNiNWs and PtNiNTs cathodes at operating conditions in the order of anode/cathode in H₂/O₂, a cell temperature of 80°C, at a) 100% RH and 1.5 bar, and b) 80% RH and 1.38 bar.

Comparison under Air:

The performance of the electrodes were also compared under Air (*figure 20*). If the current density for a given voltage is much lower than under pure O₂ due to the five times reduced oxygen partial pressure, the overall trends are similar. Compared to PtNiNTs electrode, The PtNiNWs electrode shows the best performance above 0.75V, so at low current density, but seems the more sensitive to flooding, while the PtNiNTs electrode shows the opposite trend and offer the best performance, better than Pt/C, below 0.6V. Compared to PtNi NSTF electrode having a much higher Pt loading and a loading of about 0.125 mg_{Pt}/cm_{geo}² and 20 cm²_{Pt}/cm²_{geo}, respectively, and which results from more than two decades of considerable efforts of research and development, our electrodes show lower absolute performance in similar operating conditions (80°C, under Air and 60%RH) [45]. However, the maximum current per specific surface that can be drawn from PtNiNTs electrodes is about 0.15 A/cm²_{Pt}, that is about 2 times higher than for NSTF. It seems to indicate that the oriented nanotubes architecture allows better O₂ accessibility compared to nanowires or nanowiskers architectures, and makes this nanostructured electrode less sensitive to flooding.

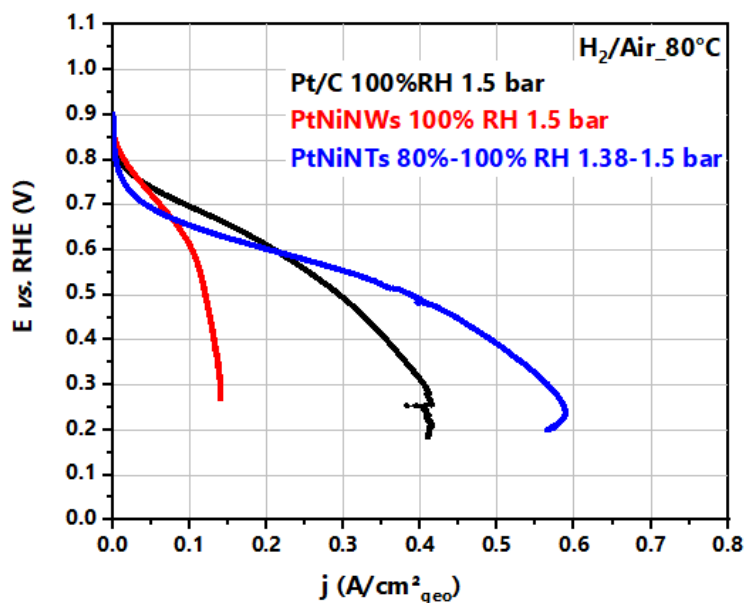


Figure 20. Comparison of H₂/Air polarization curves for the low-Pt loading cathode Pt/C (black), PtNiNWs (red) and PtNiNTs (blue).

4.2.3 Effect of Accelerated Stress Test on performance

Not only the performance of the electrodes was compared but also the stability upon Accelerated Stress Tests (AST).

The AST test was inspired from “AST Protocol from the DOE”, as described by the DOE [44] (*figure 21-a*). Drawing upon the degradation of the catalyst layer at the cathode side, the purpose of this study was to assess its durability under harsh conditions: 50K square wave potential cycles from 0.6 V_{RHE} to 1.0 V_{RHE} during 3 s, at a T_{cell} of 80°C, under H₂/N₂ at 100% RH and a total pressure of 1 bar. In this potential range, platinum oxidation and reduction occur, causing dissolution and redeposition of the catalyst, inducing low carbon corrosion (which takes place at a higher potential range >1.2 V_{RHE}).

Cyclic Voltamperometry (CV) measurements were conducted at 80°C, 100%RH before and after AST, as shown on *figure 21-b, c and d*.

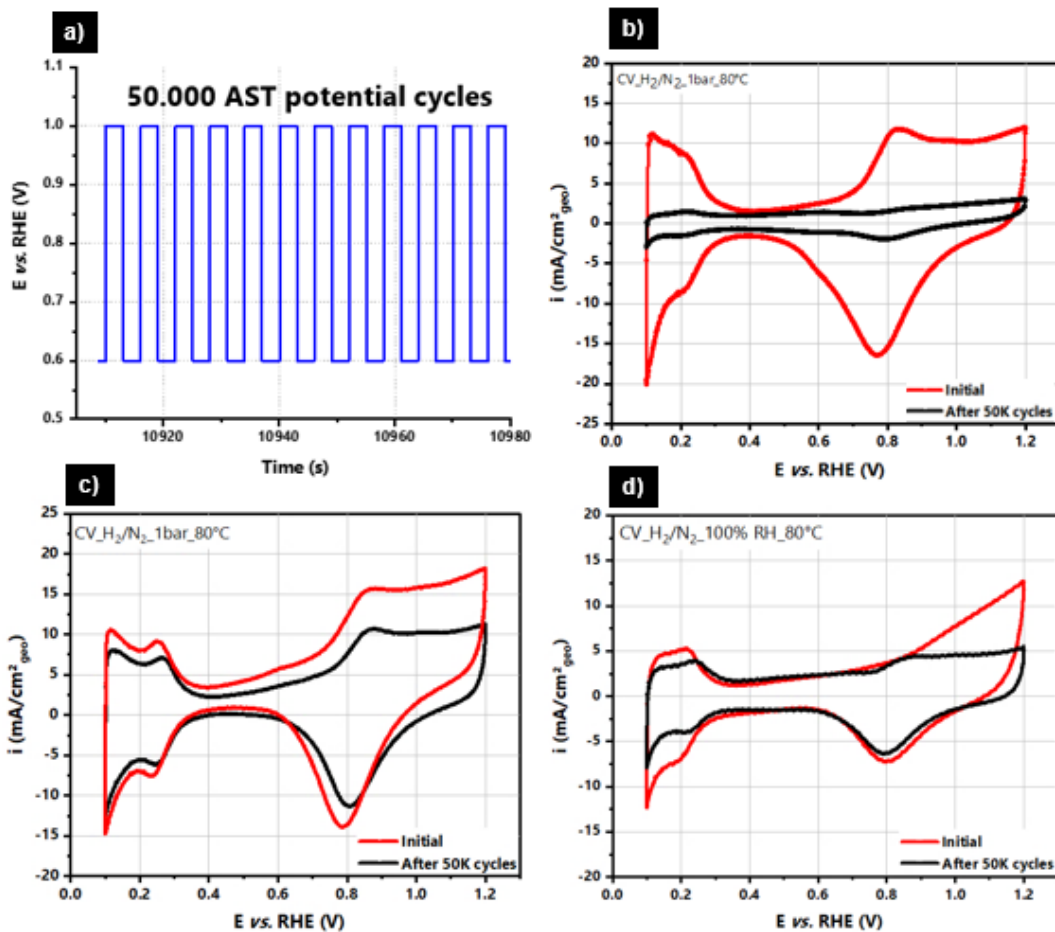


Figure 21. a) Cell voltage vs. time during voltage cycling from 0.6 V_{RHE} to 1.0 V_{RHE} to fasten the dissolution of Pt. Comparison of voltammograms before degradation and after 50K cycles conducted in H₂/N₂ at 80°C and relative humidity of 100% and a total pressure of 1 bar, recorded at a potential sweep rate of 200 mV/s, for b) Pt/C MEA, c) PtNiNWs MEA and d) PtNiNTs MEA.

We also compared the polarization curves of each MEA, before and after AST at RH values in which we got the best performances (100% RH for Pt/C, 100%RH for PtNiNWs, and 80%-100% RH for PtNiNTs), as displayed in *figure 22* below.

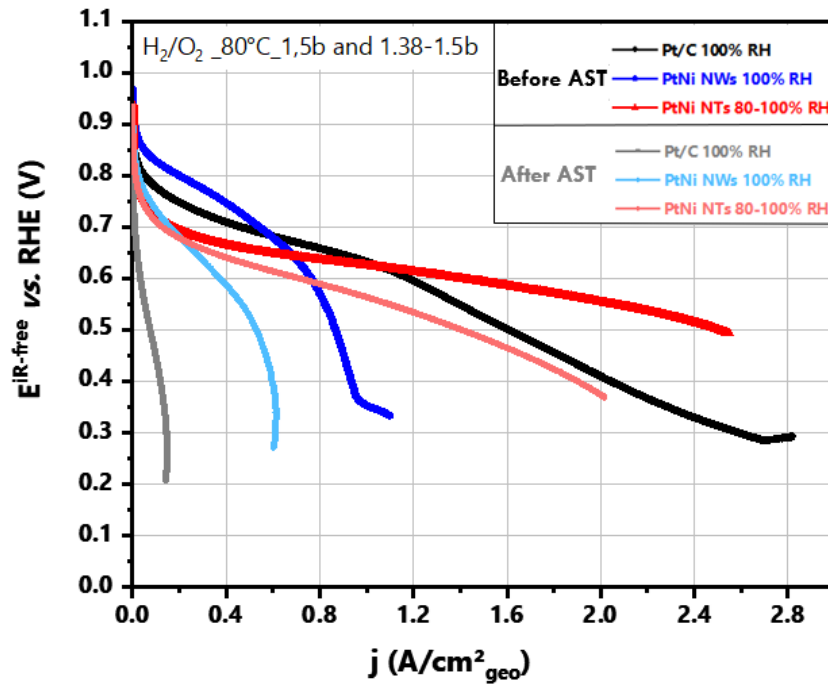


Figure 22. Comparison of fuel cell's ohmically-corrected polarization curves of Pt/C, PtNiNWs and PtNiNTs MEAs at operating conditions in H₂/O₂, cell temperature of 80°C, at different relative humidity values and total pressure (in the order of anode/cathode: 100% RH and 1.5bar, 80%-100% RH and 1.38-1.5 bar), before and after 50K load cycles.

Pt/C electrodes with low Pt loading faced drastic performance losses after AST. They have shown a poorly resistance toward aging with a significant loss of roughness (~92% loss) as displayed in *figure 21-b* above. AST towards Pt/C MEA led to a drastic drop of the H_{upd} area, yielding to lower roughness and consequently decreasing the PEMFC performance. This might be attributed mainly to the reorganization of Pt nanoparticles and their dissolution/redeposition. to form bigger NPs in the electrode, which lead to the decrease in the specific surface for the same amount of Pt. The precipitation might occur within the membrane, and thus the Pt is no longer electrically connected to the electrodes.

After 50K cycles of AST, we assumed that the drop in performance might be due to either drop in the ECSA and roughness, or either to the dissolution of catalyst, or PtNiNWs/NTs detachment from the membrane, or to Ni²⁺ ion contamination of the ionomer leading to a decrease of the accessibility of H⁺ into the catalyst, or to decay in electrochemical activity induced by *i*/ a change in the alloy's composition due to Ni dissolution or *ii*/ a change in preferred crystalline orientations of nanoparticles.

However, there are so many coupled electrochemical and physical processes that govern the performance that the comparison of the raw polarization curves of electrodes differing in the type of catalyst, nanostructure and specific electrochemical surface area can hardly allow understanding the causes of the limitations. As a first step to estimate the interest of PtNiNTs and PtNiNWs, it is beneficial to compare specific and mass activities of these electrodes and their evolution upon AST.

4.2.4 Activity before and after AST

To have a better insight into the performance and stability of the electrodes, *figure 23* summarizes the evolution of the specific activity (SA) (a) and mass activity (MA) (b) at 0.8 V_{RHE}, the ECSA (c) and the roughness (d), before and after AST. Interestingly, PtNiNWs have shown the best specific activity while PtNiNTs have shown the highest mass activity, but only after AST.

This result is not really surprising considering that the PtNiNWs behave probably similarly to bulk material that shows better specific activity compared to nanoparticles. This PtNi-based electrocatalyst nanostructure shows improved activity compared to Pt/C, as expected from the different studies in the literature. However, the enhancement compared to Pt/C, being about 13 times and 60% for specific and mass activities, respectively, before AST, that is modest compared to what has been previously reported for this latter value.

PtNiNTs electrode shows both lower specific and mass activity compared to Pt/C and PtNiNWs at the beginning of the test. There could be two explanations for that. First, while all the electrochemical surface area of the PtNiNTs can be probed using H_{upd}, a significant part might not be accessible to O₂, as about a 25% of the length of the NTs is impregnated into the membrane as shown in *figure 15*. Thus, the ECSA overestimates the real active surface area, leading to an underestimation of the specific activity. Second, it is known that for most of the PtNi nano-electrocatalyst, an in-situ dealloying step, in addition to the acid leaching after synthesis, is necessary to reach the maximum performance. The non-dealloyed catalyst can show poor activity. This is probably the case for our PtNiNTs as both the specific and mass activities are strongly enhanced after AST. The comparison of activities has demonstrated noticeable stability of PtNiNTs compared to PtNiNWs and Pt/C toward AST cycles as depicted in *figure 23-c and d* below. *Table S4* in *support information* sums up the comparison between our tested electrodes and NSTF electrodes.

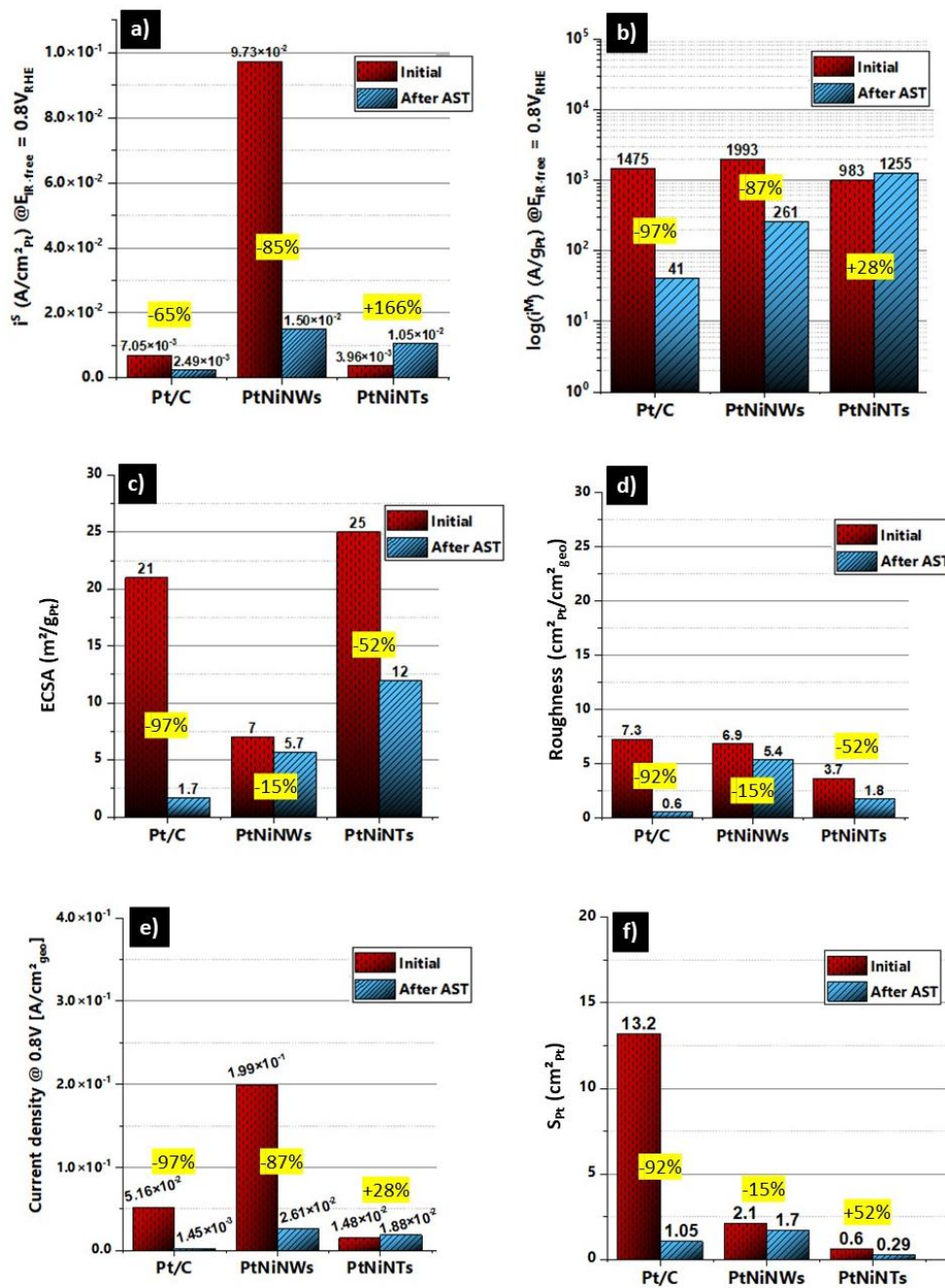


Figure 23. Comparison of the tested MEAs in this study (Pt/C, PtNiNWs and PtNiNTs as cathodes) before degradation and after 50K potential cycles in H_2/O_2 . Data recorded at $E_{iR-free}=0.8 V_{RHE}$.: **a)** Specific Activity before and after degradation, **b)** Mass Activity before and after degradation, **c)** ECSA before and after degradation, **d)** Roughness before and after degradation, **e)** Current density at $0.8V_{RHE}$ before and after degradation, and **f)** Platinum Surface before and after degradation. All resulted were obtained at $80^\circ C$, 1.5 bar, 100%RH.

5 Conclusion

In summary, we have presented a new multi-step route for elaborating oriented PtNi nanowires and nanotubes arrays devoted to the PEMFC cathode. This novel architecture of electrodes was tested in real fuel cell conditions, without the addition of the ionomer and carbon.

In real fuel cell operation, we compared the performance and the activity of different electrodes made of Pt/C, PtNiNWs and PtNiNTs. We have shown that PtNiNWs and PtNiNTs are very sensitive to RH compared to Pt/C electrodes: a low catalyst use at low RH and flooding issues at high RH.

Better performance at low current density of PtNiNWs is primarily due to the enhanced activity compared to Pt/C or PtNiNWs. However, this structure does not seem to be robust toward RH variation since it requires to be fully humidified to reach high activity but it is prone to flooding in this condition. In addition, if it is more robust toward AST compared to Pt/C, PtNiNWs are still significantly impacted by AST with significant decrease in performance induced by decay in activity. PtNiNTs electrode has low activity before aging but it is strongly enhanced, after AST most probably because of dealloying process. If also sensitive to RH variation, this nanostructure shows better performance compared to PtNiNWs when increasing current density, under both sub saturated and saturated condition, and are even better than Pt/C electrode. Thus, it seems that the organised porous structure of the PtNiNTs reduces transport limitations compared to conventional Pt/electrode. To summarize, PtNiNWs offered the best specific activity while the PtNiNTs best stability toward AST, is less sensitive to flooding and offers lower transport limitations.

Further analysis should be carried out to fathom the ORR kinetics and transport deeply. In addition, to analyse the quantity of the dissolved Ni in the membrane, which is believed to be far less than PtNiNWs. The performance and robustness toward change in relative humidity of PtNiNTs electrodes are currently limited because of the low achievable electrochemical surface area and the misuse of catalyst because of the absence of ionomer.

In this context, this paper offered a fresh and broader perspective for NTs (with post-processing optimization) as a promising route to be more investigated. Further experiments on larger nanotubes arrays are needed to better understand the behaviour of these structures. The integration of ionomer while increasing the surface area, GDL optimization and integration of an intermediate layer between the electrode and the GDL, as for NSTF could help to limit or avoid flooding at high relative humidity.

REFERENCES

- [1] IEA (2021), Greenhouse Gas Emissions from Energy: Overview, IEA, Paris <https://www.iea.org/reports/greenhouse-gas-emissions-from-energy-overview>. (Accessed on 02 January 2022).
- [2] Z.W. Seh, J. Kibsgaard, C.F. Dickens, I. Chorkendorff, J.K. Nørskov, T.F. Jaramillo, Combining theory and experiment in electrocatalysis: Insights into materials design, *Science*. 355 (2017) eaad4998.
- [3] Brian D. James & J. Kalinoski, Mass Production Cost Estimation for Direct H₂ PEM Fuel Cell Systems for Automotive Applications, January (2017).
- [4] Z.-B. Wang, P.-J. Zuo, Y.-Y. Chu, Y.-Y. Shao, G.-P. Yin, Durability studies on performance degradation of Pt/C catalysts of proton exchange membrane fuel cell, *International Journal of Hydrogen Energy*. 34 (2009) 4387–4394.
- [5] A. Alaswad, A. Omran, J.R. Sodre, T. Wilberforce, G. Pignatelli, M. Dassisi, A. Baroutaji, A.G. Olabi, Technical and Commercial Challenges of Proton-Exchange Membrane (PEM) Fuel Cells, *Energies*. 14 (2021) 144.
- [6] Y. Sun, S. Polani, F. Luo, S. Ott, P. Strasser, F. Dionigi, Advancements in cathode catalyst and cathode layer design for proton exchange membrane fuel cells, *Nat Commun*. 12 (2021) 5984.
- [7] Y.-J. Wang, W. Long, L. Wang, R. Yuan, A. Ignaszak, B. Fang, D.P. Wilkinson, Unlocking the door to highly active ORR catalysts for PEMFC applications: polyhedron-engineered Pt-based nanocrystals, *Energy Environ. Sci*. 11 (2018) 258–275.
- [8] T. Asset, R. Chattot, M. Fontana, B. Mercier-Guyon, N. Job, L. Dubau, F. Maillard, A Review on Recent Developments and Prospects for the Oxygen Reduction Reaction on Hollow Pt-alloy Nanoparticles, *ChemPhysChem*. 19 (2018) 1552–1567.
- [9] X. Zhang, H. Li, J. Yang, Y. Lei, C. Wang, J. Wang, Y. Tang, Z. Mao, Recent advances in Pt-based electrocatalysts for PEMFCs, *RSC Advances*. 11 (2021) 13316–13328.
- [10] Z.-B. Wang, P.-J. Zuo, Y.-Y. Chu, Y.-Y. Shao, G.-P. Yin, Durability studies on performance degradation of Pt/C catalysts of proton exchange membrane fuel cell, *International Journal of Hydrogen Energy*. 34 (2009) 4387–4394.
- [11] S. Cherevko, N. Kulyk, K.J.J. Mayrhofer, Durability of platinum-based fuel cell electrocatalysts: Dissolution of bulk and nanoscale platinum, *Nano Energy*. 29 (2016) 275–298.
- [12] L. Dubau, L. Castanheira, F. Maillard, M. Chatenet, O. Lottin, G. Maranzana, J. Dillet, A. Lamibrac, J.-C. Perrin, E. Moukheiber, A. ElKaddouri, G.D. Moor, C. Bas, L. Flandin, N. Caqué, A review of PEM fuel cell durability: materials degradation, local heterogeneities of aging and possible mitigation strategies, *WIREs Energy and Environment*. 3 (2014) 540–560.
- [13] M.K. Debe, R.T. Atanasoski, A.J. Steinbach, Nanostructured Thin Film Electrocatalysts - Current Status and Future Potential, *ECS Trans*. 41 (2019) 937–954.

- [14] S. Henning, J. Herranz, H. Ishikawa, B.J. Kim, D. Abbott, L. Kühn, A. Eychmüller, T.J. Schmidt, Durability of Unsupported Pt-Ni Aerogels in PEFC Cathodes, *J. Electrochem. Soc.* 164 (2017) F1136–F1141.
- [15] S.A. Mauger, K.C. Neyerlin, S.M. Alia, C. Ngo, S.K. Babu, K.E. Hurst, S. Pylypenko, S. Litster, B.S. Pivovar, Fuel Cell Performance Implications of Membrane Electrode Assembly Fabrication with Platinum-Nickel Nanowire Catalysts, *J. Electrochem. Soc.* 165 (2018) F238–F245.
- [16] S. Galbiati, A. Morin, N. Pauc, Supportless Platinum Nanotubes Array by Atomic Layer Deposition as PEM Fuel Cell Electrode, *Electrochim Acta* 125, (2014) 107–116.
- [17] D. C. Sabarirajan, T. Y. George, J. Vlahakis, R. D. White, I. V. Zenyuk, Atomic layer deposition of Pt nanoelectrode array for polymer electrolyte fuel cells, *J Electrochem Soc* 166, (2019) F3081–F3088.
- [18] O. Marconot, N. Pauc, D. Buttard, A. Morin, Vertically Aligned Platinum Copper Nanotubes as PEM Fuel Cell Cathode: Elaboration and Fuel Cell Test, *Fuel Cells*. 18 (2018) 723–730.
- [19] M. Fontana, R. Ramos, A. Morin, & J. Dijon, Direct growth of carbon nanotubes forests on carbon fibers to replace microporous layers in proton exchange membrane fuel cells. *Carbon*, (2021) 172, 762-771.
- [20] P. Oberholzer, P. Boillat, Local Characterization of PEFCs by Differential Cells: Systematic Variations of Current and Asymmetric Relative Humidity, *J. Electrochem. Soc.* 161 (2014) F139–F152.
- [21] G. E. Thompson, "Porous anodic alumina: fabrication, characterization and applications," *Thin solid film*, 297 (1997), 192.
- [22] W. Lee, S-J. Park, Porous Anodic Aluminum Oxide: Anodization and Templated Synthesis of Functional Nanostructures, *Chem. Rev.* (2014), 114, 7487–7556.
- [23] J.P. O’Sullivan, G.C. Wood, N.F. Mott, The morphology and mechanism of formation of porous anodic films on aluminium, *Proceedings of the Royal Society of London. A. Mathematical and Physical Sciences*. 317 (1970) 511–543.
- [24] H. Masuda, H. Yamada, M. Satoh, H. Asoh, M. Nakao, T. Tamamura, Highly ordered nanochannel-array architecture in anodic alumina, *Appl. Phys. Lett.* 71 (1997) 2770–2772.
- [25] C.T. Sousa, D.C. Leitao, M.P. Proenca, J. Ventura, A.M. Pereira, J.P. Araujo, Nanoporous alumina as templates for multifunctional applications, *Applied Physics Reviews*. 1 (2014) 031102.
- [26] T. Gorisse, L. Dupré, P. Gentile, M. Martin, M. Zelsmann, D. Buttard, Highly organised and dense vertical silicon nanowire arrays grown in porous alumina template on <100> silicon wafers, *Nanoscale Res Lett.* 8 (2013) 287.
- [27] A.P. Li, F. Müller, A. Birner, K. Nielsch, U. Gösele, Hexagonal pore arrays with a 50–420 nm interpore distance formed by self-organization in anodic alumina, *Journal of Applied Physics*. 84 (1998) 6023–6026.

- [28] W. Lee, K. Nielsch, U. Gösele, Self-ordering behavior of nanoporous anodic aluminum oxide (AAO) in malonic acid anodization, *Nanotechnology* 18 (2007), 475713.
- [29] H. Masuda, M. Satoh, Fabrication of Gold Nanodot Array Using Anodic Porous Alumina as an Evaporation Mask, *Jpn. J. Appl. Phys.* 35 (1996) L126.
- [30] A. Lahmar, G.H. Lee, M. Cailler, C. Constantinescu, Adhesion studies of magnetron sputtered copper films on steel substrates: Effects of heat treatments, *Thin Solid Films*. 198 (1991) 115–137.
- [31] D.M. Mattox, Thin film metallization of oxides in microelectronics, *Thin Solid Films*. 18 (1973) 173–186.
- [32] H. Han, S.-J. Park, J.S. Jang, H. Ryu, K.J. Kim, S. Baik, W. Lee, In Situ Determination of the Pore Opening Point during Wet-Chemical Etching of the Barrier Layer of Porous Anodic Aluminum Oxide: Nonuniform Impurity Distribution in Anodic Oxide, *ACS Appl. Mater. Interfaces*. 5 (2013) 3441–3448.
- [33] L.F. Marsal, L. Vojkuvka, P. Formentin, J. Pallarés and J. Ferré-Borrull, "Fabrication and optical characterization of nanoporous alumina films annealed at different temperatures", *Optical Materials* 31 (2009), 860–864
- [34] K. Nielsch, J. Choi, K. Schwirn, R.B. Wehrspohn, U. Gösele, Self-ordering Regimes of Porous Alumina: The 10 Porosity Rule, *Nano Lett.* 2 (2002) 677–680.
- [35] M.P. Proenca, C.T. Sousa, J. Ventura, M. Vazquez, J.P. Araujo, Ni growth inside ordered arrays of alumina nanopores: Enhancing the deposition rate, *Electrochimica Acta*. 72 (2012) 215–221.
- [36] K. Nielsch, F. Müller, A.-P. Li, U. Gösele, Uniform Nickel Deposition into Ordered Alumina Pores by Pulsed Electrodeposition, *Advanced Materials*. 12 (2000) 582–586.
- [37] P. Benaben, F. Durut, Electrolytic nickel coating, *Techniques de l'Ingénieur M1611* (2003).
- [38] George A. Di Bari, Book: Electrodeposition of nickel, *Modern Electroplating*, Fifth Edition Edited by Mordechai Schlesinger and Milan Paunovic, (2010) 79–114.
- [39] S.M. Alia, C. Ngo, S. Shulda, M.-A. Ha, A.A. Dameron, J.N. Weker, K.C. Neyerlin, S.S. Kocha, S. Pylypenko, B.S. Pivovar, Exceptional Oxygen Reduction Reaction Activity and Durability of Platinum–Nickel Nanowires through Synthesis and Post-Treatment Optimization, *ACS Omega*. 2 (2017) 1408–1418.
- [40] C. Fan, G. Wang, L. Zou, J. Fang, Z. Zou, H. Yang, Composition- and shape-controlled synthesis of the PtNi alloy nanotubes with enhanced activity and durability toward oxygen reduction reaction, *Journal of Power Sources* 429 (2019) 1–8.
- [41] K. Chan, M. Eikerling, A Pore-Scale Model of Oxygen Reduction in Ionomer-Free Catalyst Layers of PEFCs, *J. Electrochem. Soc.* 158 (2010) B18.
- [42] E.F. Medici, I.V. Zenyuk, D.Y. Parkinson, A.Z. Weber, J.S. Allen, Understanding Water Transport in Polymer Electrolyte Fuel Cells Using Coupled Continuum and Pore-Network Models, *Fuel Cells*. 16 (2016) 725–733.

- [43] I. Liu, R., Zhou, W., Ling, W., Li, S. & Li, F. Performance optimization of ultra-low platinum loading membrane electrode assembly prepared by electrostatic spraying. *Int J Hydrogen Energy* 46, 10457–10467 (2021).
- [44] Multi-Year Research, Development, and Demonstration Plan, Protocols for Testing PEM Fuel Cells and Fuel Cell Components, 2017. https://www.energy.gov/sites/prod/files/2017/05/f34/fcto_myrd fuel_cells.pdf
- [45] A. J. Steinbach, D. F. van der Vliet, A. E. Hestera, J. Erlebacher, C. Duru, I. Davy, M. Kuznia, and D. A. Cullen, Recent Progress in Nanostructured Thin Film (NSTF) ORR Electrocatalyst Development for PEM Fuel Cells, *ECS Transactions*, 69 (17) (2015) 291-301.

AUTHORS INFORMATION

Corresponding author: arnaud.morin@cea.fr

Email	Phone Number	Organization	ORCID
othman.lagrichi@gmail.com	+33 7.51.95.90.02	CEA Liten, Grenoble	0000-0001- 9520-007X
arnaud.morin@cea.fr	+33 4.38.78.59.86	CEA Liten, Grenoble	0000-0002- 3757-9963
denis.buttard@univ-grenoble-alpes.fr	+33 4.38.78.18.22	CEA IRIG, Grenoble	0000-0002- 3117-3559

CONFLICTS OF INTEREST: All the authors listed in this work declare that they have no conflict of interest.

ASSOCIATED CONTENT

Supporting Information

The Supporting Information is available free of charge on the ACS Publications website at DOI: XXXXXX.

- Anodic Alumina Oxide template fabrication

- Details on manufacturing and characterisations of the PtNiNWs and PtNiNTs electrodes
- Corrected and uncorrected polarisation curves under O₂ and Air

Get the PDF from [here](#).

ACKNOWLEDGMENTS:

This work was supported by CEA Grenoble and Université Grenoble Alpes. Authors want to thank PTA and BCAi for clean room facilities. Also, authors are thankful for LCP lab for complete fuel cell facilities and INAC lab for materials' elaboration apparatus and structural characterization.